Terje Kanstad
Daniel Cantero
Martin Kristoffersen
Guomin Ji

NTNU
Norwegian University of Science and Technology

Report

Hollow core slabs in the assembly process - Structural behaviour and strength during positioning of elements

Trondheim – June 2023

NTNU
Norwegian University of Science and Technology
Faculty of Engineering
Department of Structural Engineering

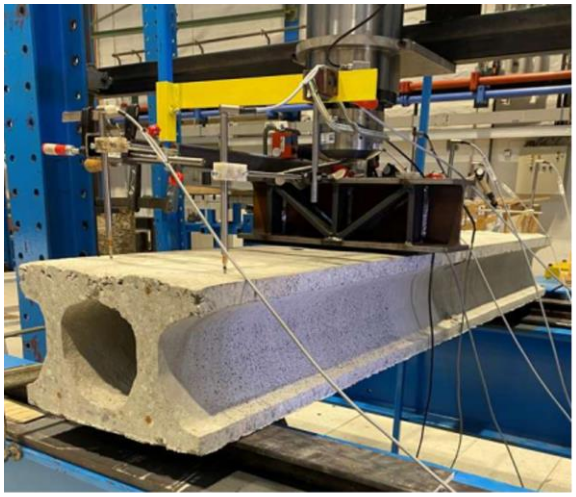

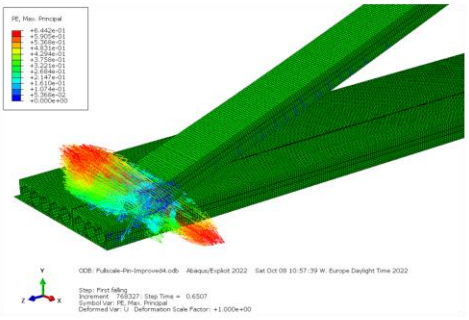

ISBN: 978-82-7482-203-0

NTNU
Norwegian University of Science and Technology

Norwegian University of Science and Technology
NTNU - Department of Structural Engineering

REPORT

Title	**Report No.**
Hollow core slabs in the assembly process – structural behaviour and strength during positioning of elements	1-23
	Date 24 January 2023 Rev. 16 June 2023
Authors Terje Kanstad, Daniel Cantero, Martin Kristoffersen and Guomin Ji	**Sign.**
	No. of pages 47

ISBN 978-82-7482-203-0

Client/Sponsor	**Availability**
Betong Norge (tidl. Norsk Betongelementforening)	Open

Summary

A series of laboratory and full-scale tests were carried out to study the structural behaviour of hollow core slabs in the assembly stage. The main objective for the project is to establish a basis for and evaluate the current regulations and practice concerning allowance of work at story levels below floors where hollow core slabs are being assembled.

The laboratory test program included material testing, static standard shear capacity tests of hollow core elements, static and impact tests of hollow core cut-outs (b/h/L = 0.4, 0.265, 2.3m), and full-scale tests with falling single hollow core elements (L = 10m) on a hollow core slab with grouted joints. The test results showed that the grouted and anchored HC slab has sufficient strength to withstand the load case.

The structural behaviour of the systems in all three test types were analysed by nonlinear finite element analyses using the software ABAQUS. The results showed that all failure cases are reasonably well described by nonlinear finite element analyses.

Indexing terms	**Stikkord**
Concrete	*Betong*
Hollow cores	*Hulldekker*
Impact load	*Støtlast*
Experiments	*Forsøksresultat*
Assembly stage	*Monteringsfasen*

Summary

A series of laboratory and full-scale field tests were carried out to study the structural behaviour of hollow core (HC) slabs in the assembly stage. The main objective by the project is to establish a basis for and evaluate the current regulations and practice concerning allowance of work at story levels below floors where HC slabs are being assembled.

The laboratory test program included material testing as compressive strength development, tensile strength and E-modulus to characterize the concrete according to the regulations, and to identify the model parameters needed for the material models applied in the nonlinear finite element analyses. Furthermore, standard quasi-static shear strength tests of two full-scale HC elements loaded with concentrated loads placed 2.5 times the hollow core's height from the support were carried out. The element-width was 1.2 m and the span-width 3,9 meters. As further basis for dynamic testing, hollow core elements of 1/3 width (=0,4 m) and approximately 2,3 m length were also tested for quasi-static shear failure. Comparisons with the regulations (Eurocode 2) showed that the investigated HC elements have a considerable additional safety margin.

The dynamic laboratory tests were carried out in the "kicking machine", designed and developed to emulate for instance car-crash and dropped objects, on HC elements with 1/3 width (0.4 m) and length 2.3 m as used in the static test. These dynamic tests showed that single hollow cores are sensitive to rigid falling objects that do not absorb energy during the impact.

The full-scale tests with one single full-width HC element falling on a floor with grouted joints, finished connections, and one restrained edge were carried out at Contiga's precast concrete element factory in Stjørdal. The floor had dimensions b/h/L=3.6 m, 0.265 m, 10.0 m (consisted of three parallel elements). The falling HC elements in the two first tests had dimensions (b/h/L=1.2 m, 0.265 m, 10.0 m), while the falling element in the last test had reduced length (L=9.7 m). The drop height was 3.2 m for the first two tests, and 3.6 m for the third. The test results showed that the grouted and anchored HC slab has sufficient strength to withstand the load case in question.

The structural behaviour of the systems in all three test types were analysed by nonlinear finite element analyses using the software ABAQUS with the material model called "Concrete Damaged Plasticity". The results showed that all failure cases are reasonably well described by nonlinear finite element analyses, and therefore a general conclusion is that the program system with its applied methodologies is capable of simulating the structural behaviour of the systems well.

Table of Contents

1. Introduction

1.1. Background

Following the well-known and serious accidents involving precast concrete elements in Norway at Brattøra, Trondheim (2012) and Nydalen, Oslo (2012), critical questions were raised regarding the stability of hollow core (HC) slab systems in the assembly stage. Although *Betong Norge* (previously *Betongelement-foreningen*) carried out investigations opposing this, serious doubts concerning the question have been claimed within the construction industry. In addition to economic consequences, the uncertainty has led to distortion of competition among industrial actors.

To establish a research-project was therefore suggested with purpose to evaluate the accidental risk of the assembly process and the structural behaviour of the process when hollow core elements are losing their support and consequently falling down on grouted and anchored hollow core slabs below. Furthermore, the board of *Betong Norge* suggested that such a project should be carried out as a collaboration between the hollow core producers and NTNU, Department of structural engineering involving both the Concrete group and SIMLab due to the obvious need for broad competence.

During the spring of 2021 a meeting between IPHA (International Prestressed Hollow core Association) and related Nordic associations was held, where it was disclosed that there are no known accidents in addition to those above mentioned. It is therefore concluded that this is a Norwegian case because there are no cases in the Nordic countries nor in other countries adjoined to IPHA similar to the accidents at Brattøra (2012) or Nydalen (2012). The performed fullscale test consisted of two cases: The planned Fall 1 and the unintended Fall 2, and, although the results from the second case are also interesting, a fall like that has never occurred in real life.

During the summer 2021 the scope was agreed upon, and a project group established. Later, in the autumn, the board of *Betong Norge* decided that the project should be carried out with proportional funding from the Norwegian hollow core producers. In December 2021/January 2022, the contract with NTNU was signed, while the project was carried out during 2022.

The project group has been composed by the following persons:

Terje Kanstad, NTNU
John-Erik Reiersen, Concrete Norway
Magne Lysberg, Concrete Norway
Martin Kristoffersen, SIMLab, NTNU
Tore Børvik, SIMLab, NTNU
Daniel Cantero, NTNU
Lars Langdal, Contiga AS
Geir Udahl, Contiga AS
Asbjørn Hermstad, SPENNCON AS
Guomin Ji, NTNU, Gjøvik
Chen Lin, NTNU, Gjøvik
Paal O Kjekstad, MSc, NTNU
Ole Johan G Løseth, MSc, NTNU

1.2. Objectives

The main objective for the project is to investigate the structural behaviour, i.e. aspects related to the strength, stability and safety of hollow core slabs in the assembly stage. The investigated case is one single hollow core element falling down on a finished (i.e. anchored and grouted) hollow core floor. The fall is assumed to be caused by failure at one support.

One more specific objective is to enlighten the problem and establish a foundation for theoretical investigations and considerations by carrying out a series of relevant experiments. The intention is to benchmark a calculation methodology based on the Nonlinear Finite Element Method towards the experimental behaviour to support the evaluation, and to make it possible to generalize the experimental results to be able to predict the outcome of other relevant cases.

A second specific objective is to establish a common understanding of the structural behaviour and give recommendations for approval, disapproval or further development of the current regulations and practice for the assembly process of precast hollow core slabs.

2. Experimental work and results

2.1. Material testing

Material tests were conducted on the concrete used to cast the hollow core slabs. Cubes with 100 mm sides and cylinders with diameter 100 mm and height 200 mm were cast in smooth steel moulds. Cube compression tests, cylinder compression tests, and tensile splitting tests were performed at D_t days after casting. The tests provide the cylinder compressive strength f_{cyl}, the cube compressive strength f_{cube}, the tensile splitting strength f_{ts}, and the Poisson ratio ν. These results, along with the measured density ρ, are given in Table 1. Further, some cylinders were used to measure Young's modulus $E_{c,S}$, or, more precisely, the secant modulus. The cylinder is compressed cyclically between lower and upper stress limits of 1/10 and 1/3 of the compressive strength. The secant modulus is determined based on the relative stress $\Delta\sigma_S$ and the relative strain $\Delta\varepsilon_S$ between the two limit states,

$$E_{c,S} = \frac{\Delta\sigma_S}{\Delta\varepsilon_S} \tag{1}$$

All tests were carried out in accordance with relevant standards [1] using a fully automated Toni Tech 3000 kN load controlled rig at a load rate of 0.6 MPa/s for the compression tests, and 0.05 MPa/s for the tensile splitting test.

Table 1 Material test results, where the final row shows the average values from tests at $D_t \approx 28$ *days.*

D_t (days)	Shape	f_{cyl} (MPa)	f_{cube} (MPa)	f_{ts} (MPa)	$E_{c,S}$ (GPa)	ρ (kg/m^3)	ν (-)	DIC?
10	cylinder	41.8	-	-	25.6	-	-	-
11	cylinder	43.7	-	-	28.7	-	-	-
11	cylinder	45.8	-	-	-	-	-	-
14	cube	-	57.6	-	-	-	-	-
14	cube	-	57.2	-	-	-	-	-
14	cube	-	56.2	-	-	-	-	-
26	cylinder	49.3	-	-	30.7	2500	-	Fig
26	cylinder	48.7	-	-	30.0	2510	-	Fig
27	cylinder	48.8	-	-	-	2490	-	Fig
27	cylinder	-	-	4.09	-	2530	-	Fig
28	cylinder	-	-	4.01	-	2530	-	Fig
28	cylinder	-	-	4.09	-	2520	-	Fig
31	cube	-	61.5	-	-	2560	0.25	Fig
31	cube	-	58.0	-	-	2570	0.20	Fig
31	cube	-	60.0	-	-	2560	0.23	Fig
Avg.	**-**	**48.9**	**58.8**	**4.06**	**30.4**	**2530**	**0.23**	**-**

In addition, digital image correlation (DIC) was used to estimate the stress-strain curves of the material, indicated by the final column in Table 1. The strains were measured by tracking the motion of so-called subset pairs on the surface of each specimen. The specimens are painted with a speckled pattern as shown in Figure 1, enabling the DIC code to track the displacements from one image to the next. The subset placements are shown in Figure 1(a) for the cylinder compression test, in (b) for the cube compression test and in (c) for the tensile splitting test. The length l, height h, and diameter d measured as

the distance between the subset pairs were used to estimate the engineering strains ee in each respective test,

$$e_{\text{cyl}} = \frac{\ell - \ell_0}{\ell_0}, \qquad e_{\text{cube}} = \frac{h - h_0}{h_0}, \qquad e_{\text{ts}} = \frac{d - d_0}{d_0} \tag{2}$$

in which subscript "0" indicate initial values of the corresponding measurement. The engineering stress S is found by dividing the logged force by the initial cross-sectional area A_0 across which the load acts. The resulting engineering stress-strain curves are thus shown in Figure 2. The data shown are the averages of the strain as measured by three subset pairs as indicated in Figure 1.

Naturally, some noise is present in these measurements because the deformations are so small. For the compression tests in Figure 2(a) and (b) there is some noise, but it is very small compared with the tensile splitting data in (c). The noise is much more pronounced in the latter because the tensile strains are one order of magnitude lower compared with the compressive strains.

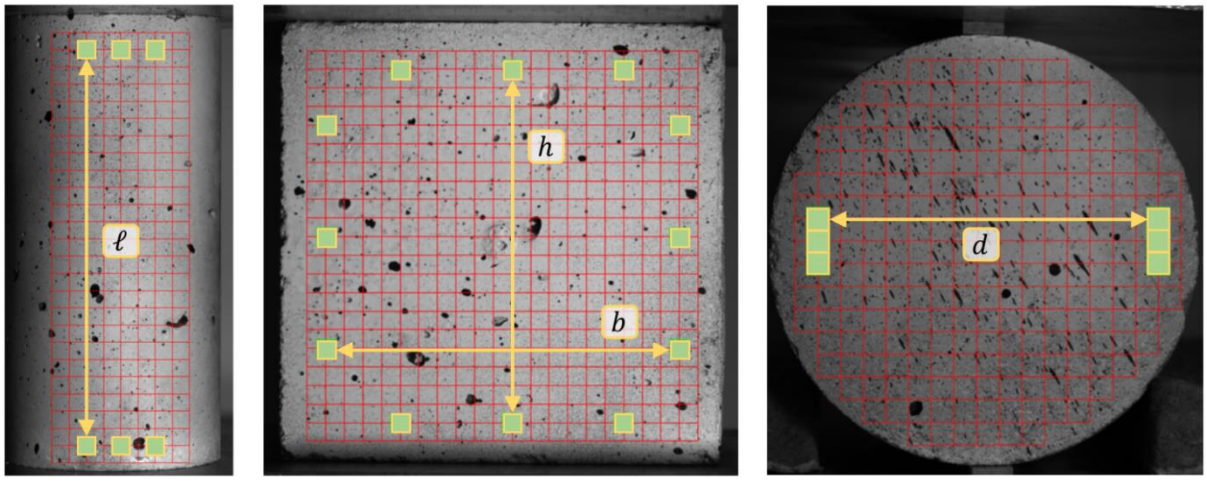

(a) cylinder (b) cube (c) cylinder (tensile splitting)

Figure 1: Measurements using subsets in the DIC code eCorr [2].

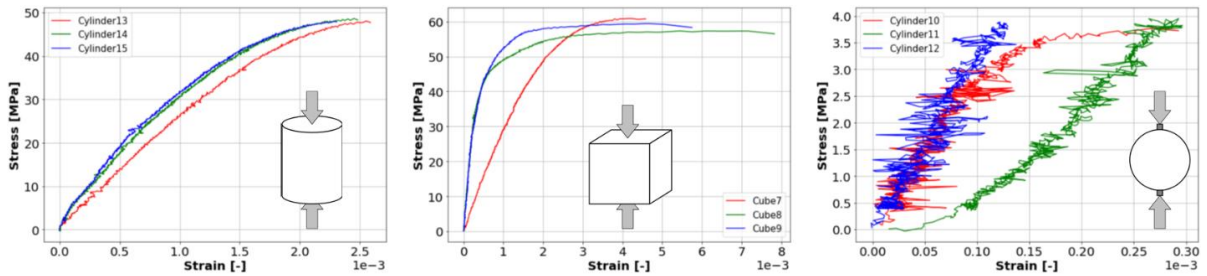

(a) cylinder (b) cube (c) tensile splitting

Figure 2: Engineering stress-strain curves obtained from DIC for (a) cylinder compression tests, (b) cube compression tests, and (c) tensile splitting tests.

As observed from Table 1 and Figure 2, the data produced appears consistent and reproducible. An exception might be cube 7 in Figure 2(b), but this could be caused by misplaced subsets and warrants

further investigation. The tensile splitting curves are naturally more scattered. It is, however, the peak load that is of interest in this case, and the peak load is quite consistent. For now, we conclude that the compressive strength is consistent across the specimens and sample dates. Average values of the tests performed around 28 days after casting can be found in the bottom row of Table 1.

2.2. Static tests

After the concrete material had been characterized, the next step was to perform static tests on finished hollow core elements. With the goal of describing the static behaviour of the fabricated elements, two different static tests were planned. First, single HC elements were tested according to the standardized procedure described in [3]. The second type of test investigated smaller cut-outs of the elements, of shorter span and approximately 1/3 of the cross-section. Both tests were performed multiple times to capture the underlying variability usually found in the experimental testing of large concrete elements.

The dimensions of the cut-outs were defined by the geometrical constraints of the dynamic testing equipment (described in Section 2.3). Therefore, the results from the static tests of the cut-outs validate the numerical model, which eventually could be further refined with the results from the dynamic tests.

Static test of single HC elements

Two HC elements of 4 m length and 265 mm height were tested to failure. The experimental configuration and loading procedure were conducted as specified in [3] (Figure 3). In this procedure, the HC elements were slowly incrementally loaded up to failure. In the last part of the test displacement control was applied. The position of the load was closer to one of the supports (662.5 mm=2.5h) ensuring that the element would break by shear failure. The elements deformations were recorded using LVDTs (linear variable differential transformers) at the supports, mid-span and near the loading point.

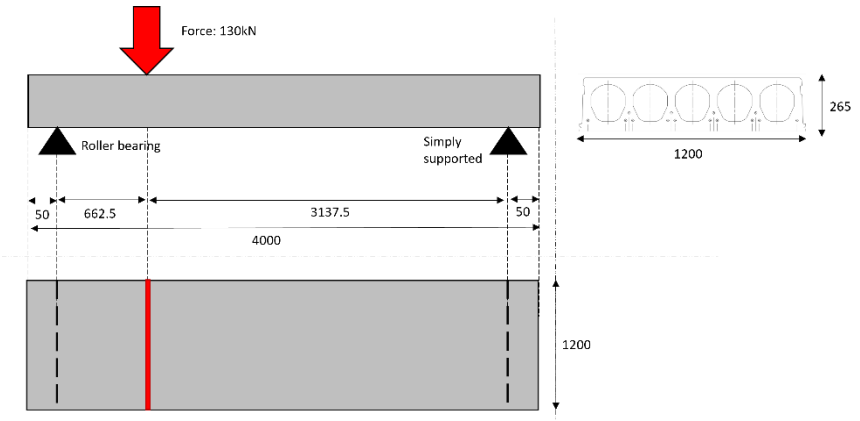

Figure 3: Static test configuration of HC elements according to in EN-1168

The same test was repeated for two identical elements. In both elements shear failure was observed for values of the load equal to 219 kN and 204 kN. The elements after failure displayed a major crack going from the line of load to the underside of the element near the support (see Figure 4). The observed crack pattern could be defined as the typical shear failure. The reported capacities and failure mechanisms were as expected, confirming that the prefabricated elements had been fabricated according to the standard. The experimental results are compared to capacities according to Eurocode 2 in Section 3.1.

Figure 4: Observed cracking after failure shear failure of HC element testing

Static test of HC cut-outs

The second type of static tests were performed on cut-outs, corresponding to approximately 1/3 of the HC elements width and spanning 2.3 m long (Figure 5). In total 8 tests were carried out. These are the same type of elements that were used in the dynamic test. The dimensions of the cut-out were defined by the maximum possible element size to be used in the dynamic test rig. Therefore, static tests of this element type were used to validate the numerical model.

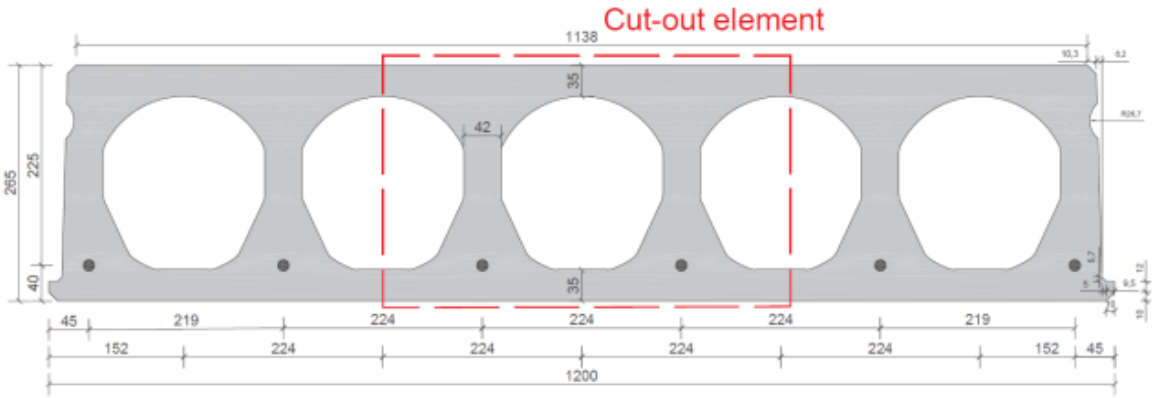

Figure 5: Cross-section of the cut-out element with respect to the original HC element

The cut-outs were positioned in a simply supported configuration for the static tests (Figure 6). The testing equipment applied a quasi-static (slowly increasing) load from the loading cell with a rounded tip to the tested element. The rate of load increase was constant throughout a single test. To ensure that no dynamic effects were observed during the testing slow loading rates and displacement control were used (10 mm/h to 20 mm/h). The load was increased until the element failed. Vertical displacements were measured at 8 different locations using LVDTs located at sections at the supports, near the loading point and at mid-span. Also, the testing equipment provided the applied load and vertical displacement at the load. In addition, a camara was used to record an area near the support where the shear cracks

were expected to appear. The processing of the video by digital image correlation (DIC) was used to map the cracking of the element.

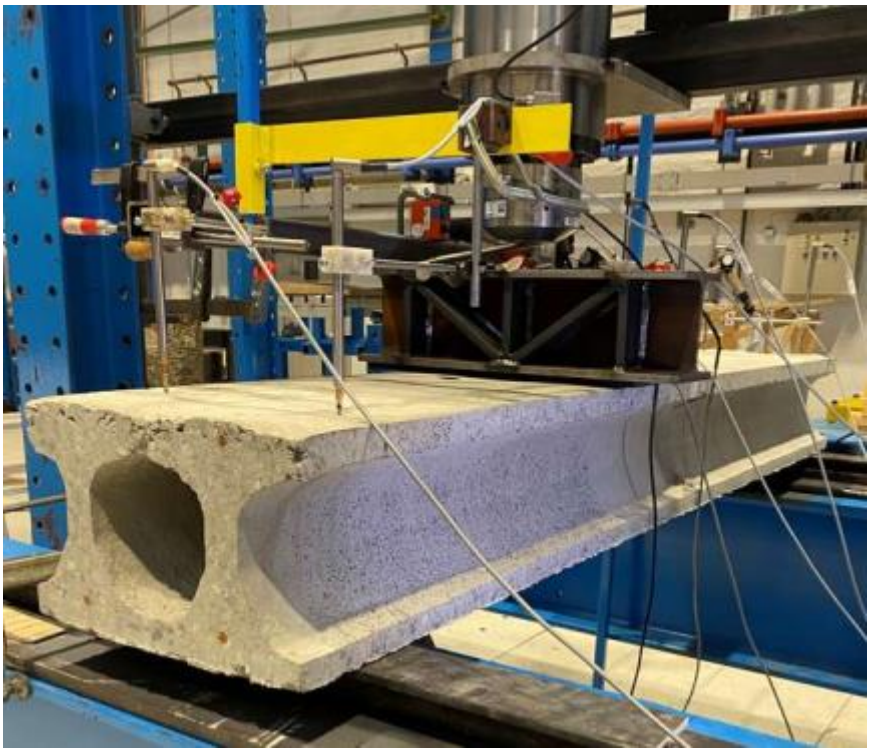

Figure 6: Static test set-up of cut-out element

The test was repeated on eight cut-out elements with four different load and support conditions. The test set-up was initially defined to ensure shear failure on the 2.3m cut-out elements. However, the testing showed that the actual shear capacity of the elements was larger than calculated, which led to bending failures of some elements. Therefore, small modifications in the geometry of the test were introduced with the goal of obtaining shear failures. In total 4 different configurations were tested performing 2 repetitions for each. The distance between the load and the nearest support was 2.5 times the element height (2.5h), 2.18h or 1.81h. Eventually, for the 8 static tests on the 2.3 m long cut-outs, 3 resulted in shear failure, and 5 in moment failure. Figure 7 shows the notation used to define the geometry of the test set-up. The adopted testing geometry and summary of the test results are provided in Table 2.

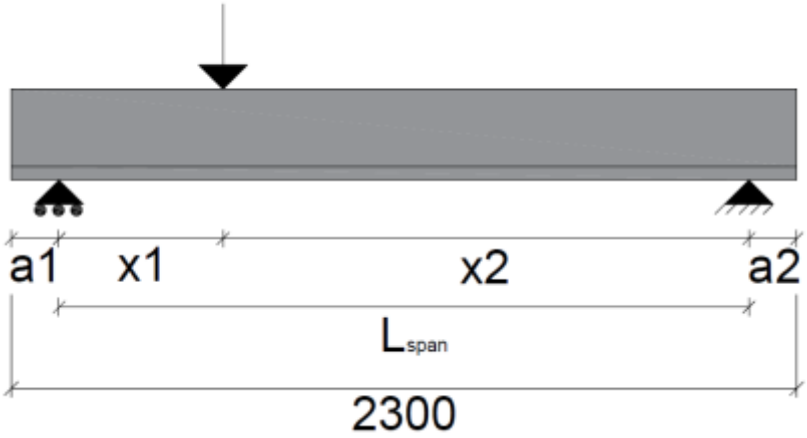

Figure 7: Dimension of static test set-up

Table 2: Summary of static test on cut-outs

Test ID	ID01	ID02	ID03	ID04	ID05	ID06	ID07	ID08
a1	140	140	140	140	140	140	50	50
a2	140	140	140	140	240	240	630	630
x1	662.5	662.5	580	580	480	480	480	480
x2	1357.5	1357.5	1440	1440	1440	1440	1440	1440
L_span	2020	2020	2020	2020	1920	1920	1620	1620
Force (kN)	127.3	116.0	123.6	119.0	107.4	113.7	112.2	117.5
Crack at (kN)	92.2	92.2	103.8	100.9	107.4	104.2	112.2	114.4
Failure	Bending	Bending	Bending	Shear	Shear	Bending	Bending	Shear

Figure 8 shows examples of crack distributions at the instance of failure as extracted by DIC. Test ID02 had a clear bending failure, while almost for the same load test ID04 presented a clear shear failure (x1 in Figure 7 reduced from 2.5h to 2.18h).

(a)

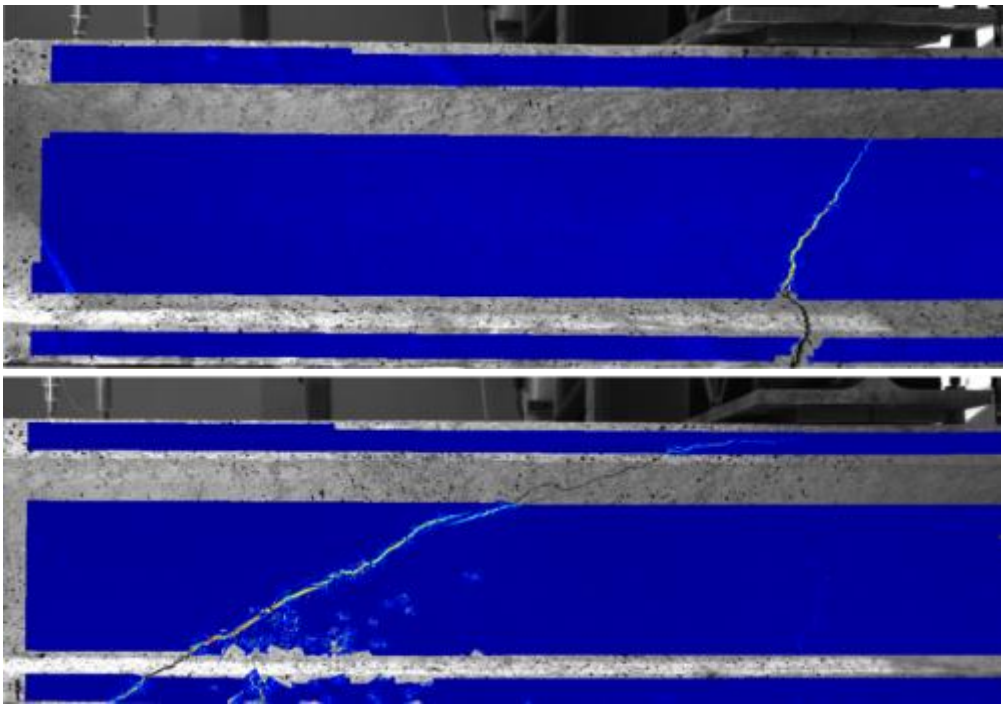

(b)

Figure 8: Crack pattern examples for (a) Bending failure of element ID02; (b) Shear failure of element ID04

2.3. Dynamic tests on hollow core cut-outs

Setup

A total of 7 dynamic component tests were performed in a pendulum accelerator, colloquially called the "kicking machine". The rig is shown in Figure 9, where the test specimen is exemplified by a bumper system, but this could be anything that fits into the rig. In this case, it is the HC cut-outs as illustrated previously in Figure 5. The rig's arm is pneumatically activated and accelerates the trolley with mass $M = 441$ kg to a specified velocity V_0 and corresponding kinetic energy $E_k = MV_0^2/2$. The nose of the trolley is adapted to the specific needs of each test and is mounted on the trolley's load cell. Two Phantom v2511 high-speed cameras – pictured in Figure 10(a) – recording at 25000 frames per seconds captured the impact. Stickers were placed on the specimens to track their motion during testing. The high-speed footage was also used to measure the initial impact velocity of the trolley.

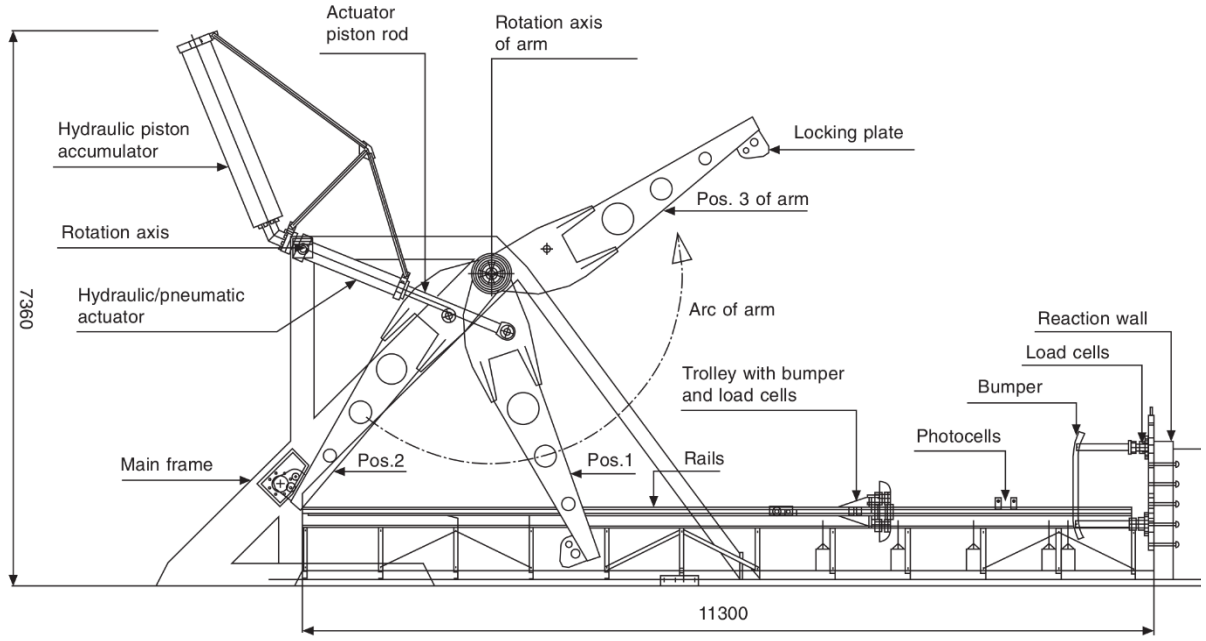

Figure 9: Test rig for dynamic impact testing [4]. The arm accelerates the trolley with the bumper.

The impact energies for these tests were determined based on the quasi-static tests, where the force-displacement curves were integrated. The resulting velocities were below what the kicking machine can reliably produce. Thus, an initial test with the lowest possible impact velocity was conducted to assess the outcome. It was then decided to pull the trolley by hand to achieve even lower impact velocities. This approach worked out well, although it was difficult to produce a precise impact velocity. For all 7 tests, the velocity was successfully measured by the high-speed cameras. The tests were labelled DHD01 to DHD07.

Like the quasi-static test, the setup consists of a simply supported hollow-core cut-out beam. The span is now 1500 mm as shown in Figure 10(b), and the specimen is mounted vertically to fit in the rig as depicted in Figure 10(c). A nose for the trolley was created to emulate the loading conditions from the quasi-static tests and connected to the trolley as shown in Figure 10(d).

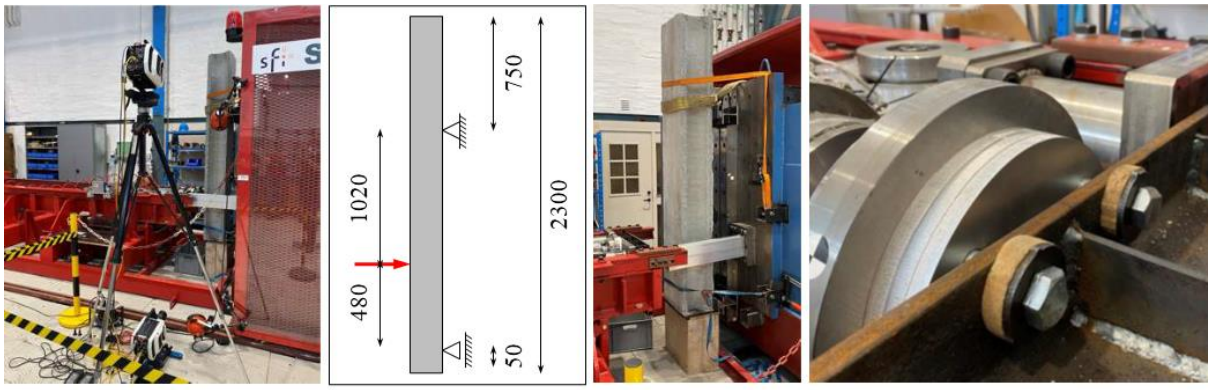

(a) cameras (b) geometry (mm) (c) setup (d) trolley connection

Figure 10: General setup of dynamic impact tests, where (a) shows the camera positions, (b) gives the geometry of the span and setup, (c) shows a picture of the test setup, while (d) shows the connection between the trolley and the nose.

Results

As for the quasi-static tests, there were failures due to both shear and bending moment (probably only cracking and no yielding of reinforcement). As Table 3 shows, the tests with the three highest velocities give a shear failure, while the four lowest velocities give moment failure (cracking). The range of velocities is not vast so this might be a coincidence, but higher velocities typically trigger more local shear failure compared with lower velocities. Further, nothing in the quasi-static test data suggests any correlation of this kind.

Table 3 Results from dynamic impact tests.

Impact test no.	(-)	DHD01	DHD02	DHD03	DHD04	DHD05	DHD06	DHD07
Velocity V_0	(m/s)	3.89	3.40	2.10	2.51	3.37	3.34	3.93
Kinetic energy E_k	(J)	3336	2549	972	1389	2504	2460	3405
Max. deformation	(mm)	21.6	15.4	3.8	6.0	9.0	9.3	25.1
Failure type	(-)	shear	shear	moment	moment	moment	moment	shear

Unfortunately, the chosen load cell was too small for the forces encountered during impact. It suffered permanent damage from the first test and was not used for subsequent tests. For this reason, only velocity and displacement data are available from the impact tests (in addition to high-speed videos) and can be found in Figure 11. The force recorded for test DHD01 peaked at about 800 kN.

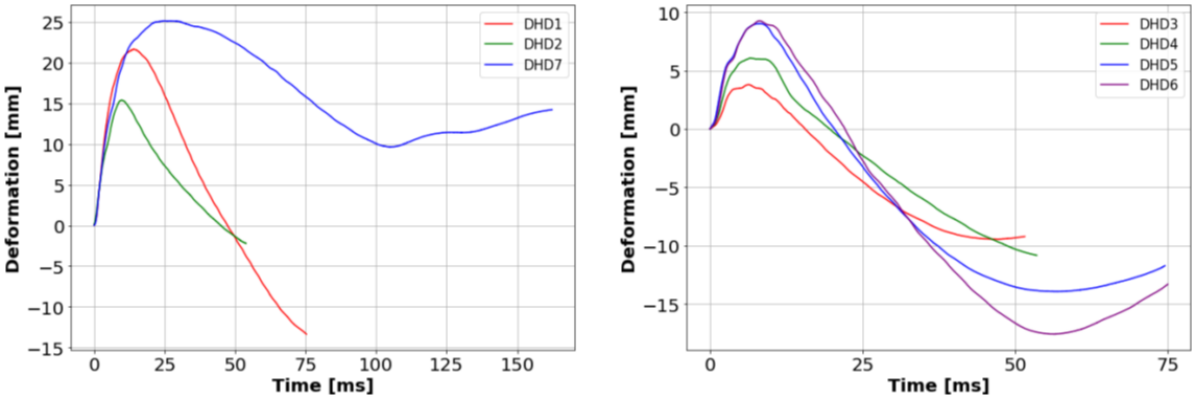

(a) Shear failures (b) Moment failures

Figure 11: Displacement vs. time for all tests, where (a) shows the specimens suffering shear failure, and (b) moment failure (cracking).

2.4. Full-Scale tests

The full-scale tests took place at the premisses of Contiga AS (Stjørdal). The intention of the tests was to study a possible construction accident with typical hollow core slab (HCS) dimensions, story-height, span-width, and boundary conditions. There were also some similarities to the reported accident in Trondheim in 2012. The idea was to study the structural behaviour and failure mechanisms of a single hollow core element falling over a finished floor. The floor consisted of 3 HC elements spanning 10 m. The two joints between the elements were grouted one week before testing. In addition, the floor was connected to the supports by a grouted connection between protruding steel bars from the supports enchased around recesses at the HC ends. The falling HC element was positioned over the floor at a typical floor height, hanging from a steel frame rig (See Figure 12).

Figure 12: Overview of full-scale experimental set-up

The experiment sequence consisted of 2 falls of the same element. During the first fall (F1), one hanger was released, and the partially hanging element impacted the floor. After some time, the other hanger was released too, producing a second fall (F2) on the same floor. This experimental set-up was repeated 3 times on three identical floors. To identify test and fall number, the following notation is adopted, indicating test number T and fall number F (e.g. T1F2 = Test 1 and Fall 2). A schematic representation of the problem with applied dimensions is given in Figure 13. Tests T1 and T2 were identical, with length of falling element (L) and story-height (H) of 10 m and 3.2 m respectively. The dimensions for T3 were slightly different (L = 9.7m, H = 3.6m).

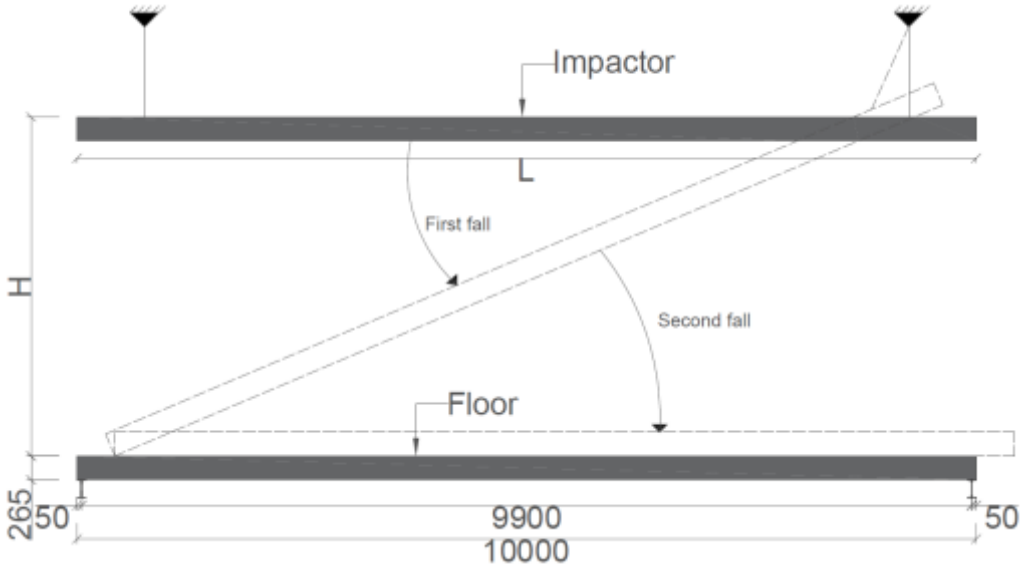

Figure 13: Schematic description of the full-scale tests

During each of the tests, several measurements were performed. High-speed camera recordings were used to track the behaviour near the support closest to the impact. High visibility indicators were placed on the floor and the falling object to enable result extraction during the video post-processing. In addition, three normal video cameras recorded the test from different perspectives. With this set up it was possible to document the location of impact and the progressive collapse of the falling element. Figure 14a is one of the images obtained from the high-speed camera that shows one instant right after impact. By processing the whole sequence of images recorded during the impact, it was possible to extract vertical deformations in time at different locations of the floor (Figure 14b). However, note that this was not always possible for all falls because of instability of the reference objects during these violent and energetic tests.

In general, the falling element showed multiple progressive shear failures in all tests during the first fall (F1), destroying the element end completely. During this failure it was recorded that the floor experienced a sequence of impacts. When the falling element first impacted the floor, the end gets destroyed. Then the element continued falling, where the new end of the element gets smashed too. This sequence is repeated multiple times (at least 5 times). The total energy of the first fall is therefore greatly dissipated in the sequence of successive element ends failures. As a result, the observed damages on the floor after the impact are almost non-existent, neither on the impact area or on the bottom face of the floor.

This indicates that the impact can be described as some type of plastic impact in which the maximum force was limited by the failure mode of the falling element, resulting in an impact with a "long" duration against the floor. The impact velocity should have been about 8 m/s. The failure response described here was positive for the possibility of the floor to withstand the impact load it was subjected to. The reason why the falling slab was damaged like this might be related to the larger mass activated in the floor (i.e. less energy transferred to the floor than in the falling slab due to impact). The presence of grouting would also affect this, both the mass and the load capacity of the floor.

For T1F1 and T2F1 the impact was close enough to the floor edge and within the range of the grouted area of the support. This might explain why no damage was observed, since that region of the floor is stronger. But also T3F1 showed no indication of damage, even when the impact was further away of the stronger grouted support connection. However, even if the floor presented no obvious damage, it might have cracked during the impact and restored immediately after the impact. Therefore, there might be some hidden damage and reduced capacity of the floor after the first fall. The experiment was not designed to be able to assess the remaining capacity of the floor after the first impact. Nevertheless, the good condition assessed by visual inspection of the floor after the first fall indicates that there was extremely low probability of the floor collapsing after the first fall.

(a)

(b)

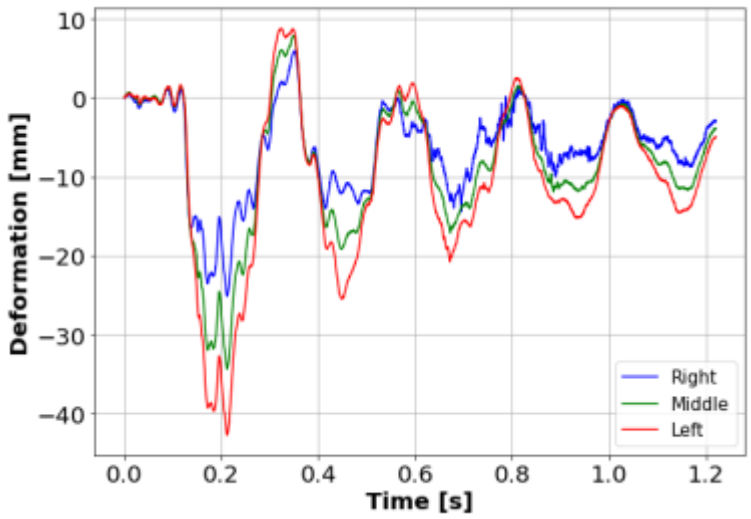

Figure14: (a) Instant of appearance of the 3rd crack on the falling element in T1F1; (b) Vertical deformations in time of various sections in the floor during T2F2. The sections Right, Middle, Left refer to the view in Figure 13.

On the other hand, the second falls resulted in more severe damages to the floor. When the falling element was released for the second fall, the element was resting on the floor on one end. Therefore, the element rotated around that supporting location and the whole element hit the floor simultaneously. The falling element did not get further damage, transferring most of the energy of the impact to the floor. In particular, for T1F2 and T2F2 the floor showed severe damages with longitudinal cracking parallel to the longitudinal joint, spanning 2/3 of element. The joints between floor elements transmitted

the energy to the neighbouring elements resulting in cracking starting from the impact location on the top developing to the bottom face below the first void of the neighbouring element as shown in Figure 16. In addition, for T3F2, the floor suffered more severe damage near the support and substantial damage of the grouting between elements.

In all three tests, and after the 2nd falls, obvious longitudinal cracking could be observed on the floor. As shown in Figure 15, both grouted joints showed these cracks on the top surface, and severe cracking (and material loss) was observed on the bottom face of the floor. This behaviour might be explained because the floor bends around both horizontal axes when loaded by the falling element. In the longitudinal direction, the floor was capable to resisting it without any distinct bending failure. However, more severe damages are observed in the transverse direction. The grouting at the joints transferred that bending from the central element to the outer elements. At those locations the floor had large moment capacities due to the local presence of two HC webs connected with the joint. Therefore, there is little bending, and most of the forces are transferred through large shear stresses. The shear capacity is exceeded producing the observed cracks in the longitudinal direction, that start at the top of the joint's grout and go diagonally towards the bottom of the HC element below the closest void. Thus, having fully grouted connections is vital for distributing the impact load to neighbouring elements.

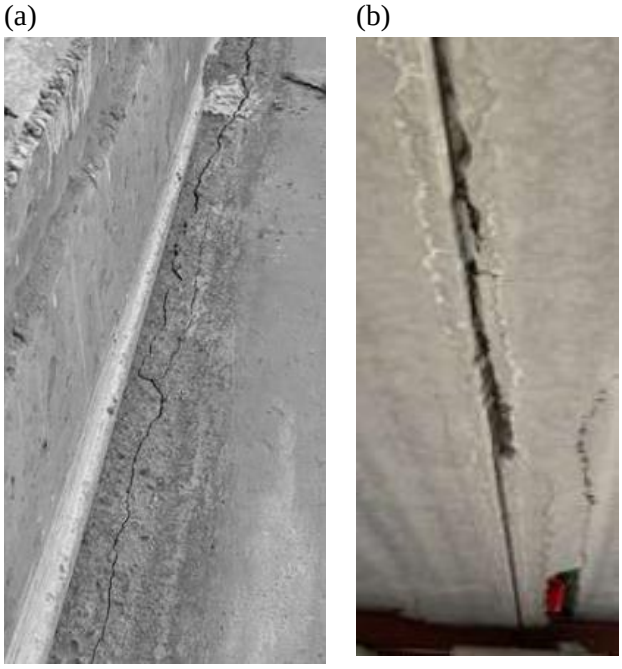

Figure 15: Longitudinal cracking (T3F2). (a) Top of floor, cracking along the grout of the joint; (b) Bottom face of floor

The large amount of energy transferred at F2 produced severe damage to the floor, as shown in Figure 16. Once the concrete is broken, the structural system dissipates energy from the impact by increased tensile forces in the strands. Energy is dissipated by overcoming the bond and friction forces between the active steel and the concrete. This mechanism was registered in the quasi-static tests by recording the strand slip at the ends of the HC elements.

(a)

(b)

Figure 16: Floor damage (T3F2); (a) Bottom face of floor with severe damage in middle and neighbouring elements; (b) Detail showing exposed prestressing strand

3. Calculation methods and results

First, calculations according to governing regulations were carried out. In order to get a better understanding of the response of hollow core slabs under various load conditions, finite element (FE) analyses were performed for static, dynamic and full-scale test by using ABAQUS.

3.1. Static test results vs regulations (Eurocode 2)

The shear capacity $V_{\mathrm{Rd,c}}$ of the hollow cores from the static tests were calculated according to Eurocode 2, Clause 6.2.2 Formulae 6.4:

$$V_{\mathrm{Rd,c}} = \frac{I \cdot b_{\mathrm{w}}}{S} \cdot \sqrt{(f_{\mathrm{ctd}})^2 + \alpha_{\mathrm{l}} \sigma_{\mathrm{cp}} f_{\mathrm{ctd}}} \tag{3}$$

In which b_w is the web width (the sum for HC), S the 1st area moment (the area above gravity center), f_{ctd} is the factored design tensile strength, σ_{cp} the axial compressive stress, while α_{l} represents the gradual development of the prestressing force.

The prescribed concrete quality (B45) was assumed, the material factors were set equal to 1.0, and the prestress was specified in accordance with information from the producer (Contiga). Figure 17 shows that all experimental results lie considerably on the safe side. As explained and discussed previously some of the cut-out elements got moment failure instead of shear failure which means that the shear capacities in some cases are larger than shown in the graph.

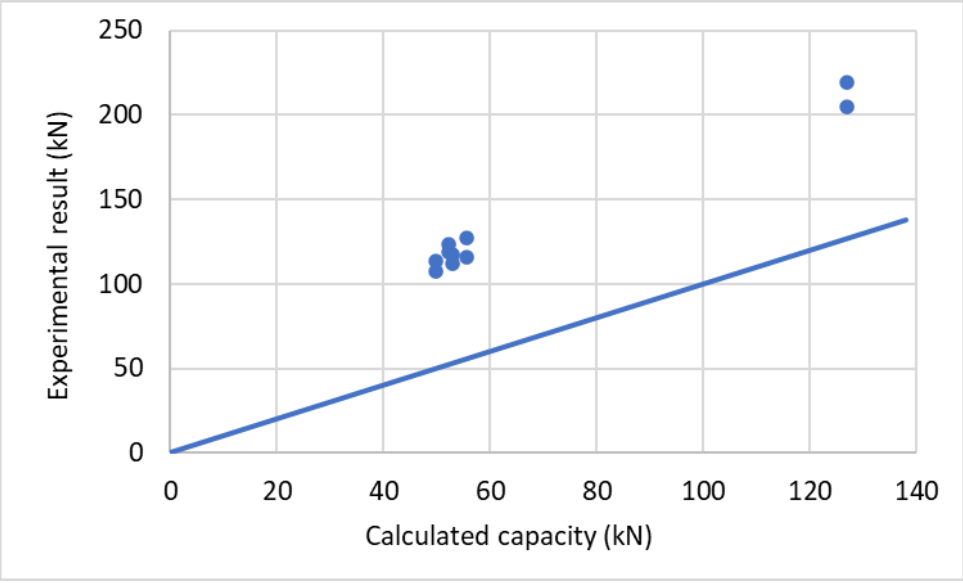

Figure 17: Experimental results versus calculated shear capacities of the tests described in Section 2.2.

3.2. Material modelling

The concrete material model used is the "Concrete damage plasticity" model (CDP model) as implemented in ABAQUS [5]. It is based on the work by Lubliner et al. [6] and by Lee and Fenves [7], and the reader is referred to those studies and the ABAQUS manual [5] for a complete description. A few key features are included here, and all parameters needed for material input in ABAQUS are mentioned. The input data used for all simulations herein are summarised in Table 4.

The model is formulated in terms of the effective stress $\overline{\sigma}$

$$\overline{\boldsymbol{\sigma}} = \frac{\boldsymbol{\sigma}}{1-d} = \mathbf{D}_0^{\mathrm{el}} : (\boldsymbol{\varepsilon} - \boldsymbol{\varepsilon}_{\mathrm{pl}}) \tag{4}$$

in which σ is the Cauchy stress tensor, D_0^{el} is the undamaged elastic stiffness tensor, d is the scalar damage, and ε and ε^{pl} the total and plastic strain tensors, respectively. The damage parameter d is composed of a compressive part d_c and a tensile part d_t which are thought to represent compressive crushing and tensile cracking, respectively. The scalars d_t and d_c are input to ABAQUS as functions of the so-called cracking strain $\tilde{\varepsilon}_t^{ck}$ and inelastic strain $\tilde{\varepsilon}_c^{in}$ in tabulated form. The equivalent plastic tensile and compressive strains $\tilde{\varepsilon}_t^{pl}$ and $\tilde{\varepsilon}_c^{pl}$, are then calculated from

$$\tilde{\varepsilon}_t^{\mathrm{pl}} = \tilde{\varepsilon}_t^{\mathrm{ck}} - \frac{d_t}{1-d_t} \cdot \frac{\sigma_t}{E_0} \tag{5}$$

$$\tilde{\varepsilon}_t^{\mathrm{pl}} = \tilde{\varepsilon}_c^{\mathrm{in}} - \frac{d_c}{1-d_c} \cdot \frac{\sigma_c}{E_0} \tag{6}$$

where E_0 is the initial undamaged Young's modulus, and σ_t and σ_c are the tensile and compressive cohesion stresses, respectively. If the stresses σ_t and/or σ_c become too large, for instance due to erroneous input or strain rate effects, $\tilde{\varepsilon}_t^{pl}$ and $\tilde{\varepsilon}_c^{pl}$ might end up being not monotonically increasing (or even negative). This generates an error message in ABAQUS [5].

The input parameter σ_{b0}/σ_{c0} in the material model is the ratio of initial equibiaxial compressive yield stress to initial uniaxial compressive yield stress, while K_c controls the shape of the yield surface in the deviatoric plane. The angle ψ is the dilatation angle in the p–q-plane, where q is the von Mises equivalent stress and p the hydrostatic pressure (positive in compression). Strain rate sensitivity is included by entering tabulated yield stress values for different strain rates, which are then interpolated linearly. The strain rate sensitivity has been input in accordance with the CEB-FIP model code [8].

To obtain representative material parameters, the cylinder test was reverse engineered until the peak experimental load. After the peak, the concrete cracks and the strain field becomes highly non-homogeneous. A cylinder with diameter 100 mm and height 200 mm was discretized using 8-node constant strain reduced integration solid elements (C3D8R in ABAQUS) with an element size of 25 mm as shown in Figure 18. This is approximately the same element size as used in the large-scale simulations, thereby reducing mesh size dependency. A 100 mm cube compression test was also modelled for verification. Two rigid plates were modelled to compress the specimen, and a time scaling factor of approximately 10^{-2} was used. No strain rate dependent data was used to maintain quasi-static conditions. The kinetic energy in the simulations was well below 1 % in all cases.

Table 4 Material data for the CDP model.

$\rho_c\rho_c$ (kg/m^3)	E_cE_c (GPa)	$\nu_c\nu_c$ (-)	
2530	36.5	0.23	
$\psi\psi$ (deg)	$\epsilon\epsilon$ (-)	$\sigma_{b0}/\sigma_{c0}\sigma_{b0}/\sigma_{c0}$ (-)	K_cK_c (-)
38	1.0	1.12	0.666

Compression hardening		Compression damage	
Yield stress (MPa)	Inelastic strain $\tilde{\varepsilon}_c^{in}\tilde{\varepsilon}_c^{in}$ (-)	Damage d_cd_c (-)	Inelastic strain $\tilde{\varepsilon}_c^{in}\tilde{\varepsilon}_c^{in}$ (-)
22.80	0	0	0
25.00	0.000081	0	0.000081
35.00	0.000452	0	0.000452
47.00	0.000900	0	0.000900
51.80	0.001300	0	0.001300
51.90	0.003400	0.110000	0.003400
30.00	0.005900	0.199851	0.005900
12.00	0.007400	0.538831	0.007400
5.00	0.011900	0.894865	0.011900

Tension stiffening		Tension damage	
Yield stress (MPa)	Cracking strain $\tilde{\varepsilon}_t^{ck}\tilde{\varepsilon}_t^{ck}$ (-)	Damage d_td_t (-)	Cracking strain $\tilde{\varepsilon}_t^{ck}\tilde{\varepsilon}_t^{ck}$ (-)
3.2596	0	0	0
4.0600	0.00006900	0	0.00006900
3.0508	0.00032085	0.406411	0.00033209
1.4036	0.00055953	0.696380	0.00055953
0.3712	0.00136991	0.920389	0.00136991
0.0928	0.00217346	0.980093	0.00217346

$\sigma_{b0}/\sigma_{c0}K_c\psi pqqp$The results are given in terms of engineering stress and engineering strain in Figure 18. We see that both the cylinder and cube compression tests are well represented by the calibrated material and should thus give an accurate representation of the material in the component and full-scale tests.

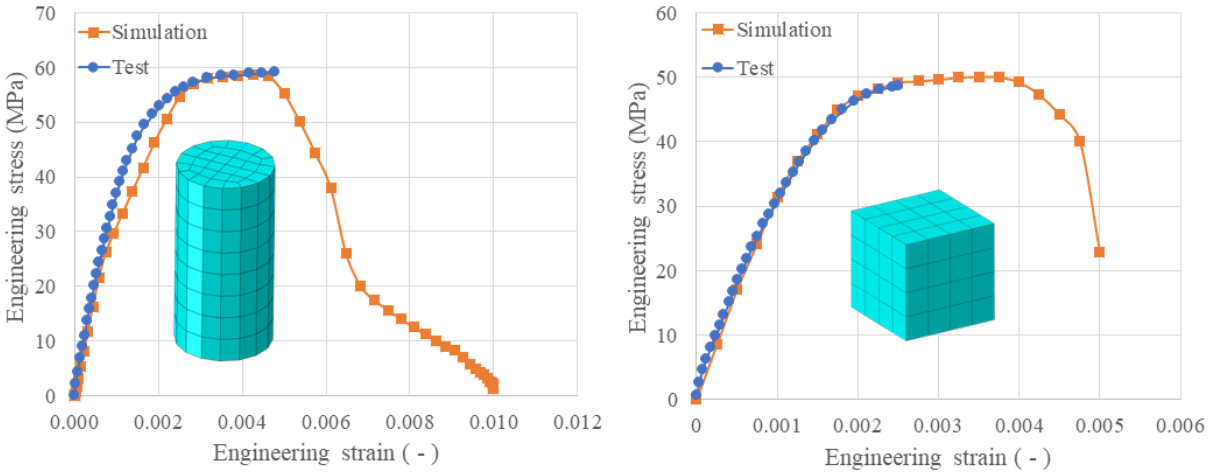

Figure 18. Material test results with simulations for cylinder (left) and cube (right).

3.3. Finite element (FE) models of the simply supported hollow core slabs

The prestressed tendons were modelled by rebar truss elements of type T3D2 which were embedded in concrete with perfect bonding. The pre-tension was introduced by predefined temperature changes in the tendons.

The HCS were modelled by solid elements of type C3D8R, and the element mesh is illustrated in subsequent figures together with result plots. A continuum, plasticity-based, damage model as described in Section 3.2 was used for concrete, and the material properties for the concrete damage plasticity model are presented in Table 4. The contact between the loading plate and the top surface of HCS was defined by surface-to-surface contact.

The static test setup and the FE model of the simply supported HCS are shown in Figure 19. The boundary conditions of the support steel plates are described in Table 5. The static loads were applied in three steps in the simulation:

1) The gravity was applied initially.
2) The targeted prestress was applied on the tendons through temperature changes.
3) The concentrated load was applied on the slab through displacement control of the loading plate.

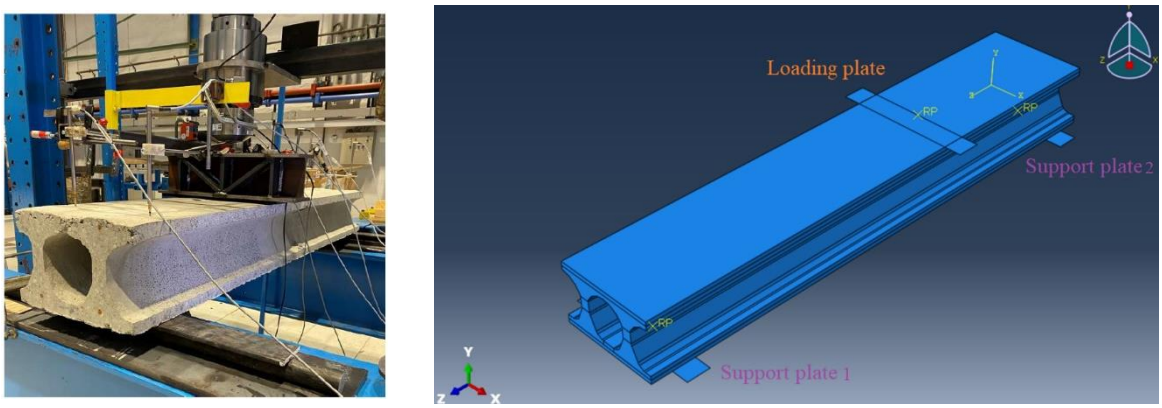

a) Static test b) FE model

Figure 19: Simply supported hollow core slab

Table 5: Boundary condition of the support plates

Support	Boundary conditions
Plate 1	Fixed in translation in X and Y direction and rotation about Y and Z axis
Plate 2	Fixed in translation in X, Y and Z direction and rotation about Y and Z axis

3.4. Finite element models of the dynamic impact test

The dynamic impact test setup and the FE model are shown in Figure 20. The strain rate dependent material properties according to CEB-FIP Model Code 90 as shown in Figure 21 were used in the simulations.

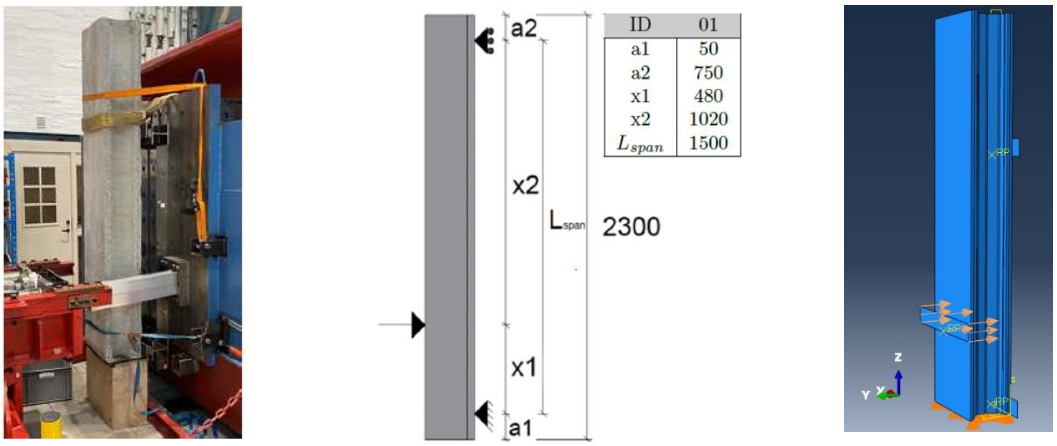

a) Dynamic impact testing b) Idealized impact test setup c) FE model

Figure 20: Hollow core slab in dynamic impact test

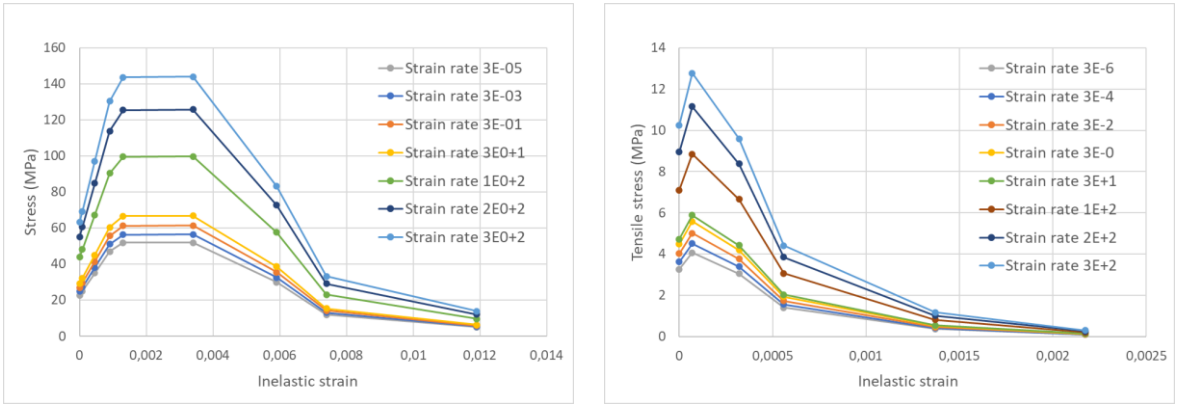

a) Compressive strength b) Tensile strength

Figure 21: Strain dependent Stress-Inelastic strain relationship

For a given strain rate the compressive strength was estimated from the following equations:

$f_{c,imp}/f_{cm} = (\dot{\varepsilon}_c/\dot{\varepsilon}_{co})^{1.026\alpha_s}$ for $|\dot{\varepsilon}_c| \leq 30s^{-1}$

$f_{c,imp}/f_{cm} = \gamma_s(\dot{\varepsilon}_c/\dot{\varepsilon}_{co})^{1/3}$ for $|\dot{\varepsilon}_c| > 30s^{-1}$

With $\log\gamma_s = 6.156\alpha_s$-2

Where $\dot{\varepsilon}_c$ is the strain rate (s^{-1})

$\dot{\varepsilon}_{co} = -30 \times 10^{-6} s^{-1}$

$\alpha_s = \frac{1}{5+9f_{cm}/f_{cm0}}$ with $f_{cm0} = 10\text{MPa}$

For a given strain rate the tensile strength was estimated from the following equations:

$f_{ct,imp}/f_{ctm} = (\dot{\varepsilon}_{ct}/\dot{\varepsilon}_{cto})^{1.016\delta_s}$ for $\dot{\varepsilon}_{ct} \leq 30s^{-1}$

$f_{ct,imp}/f_{ctm} = \beta_s(\dot{\varepsilon}_{ct}/\dot{\varepsilon}_{cto})^{1/3}$ for $\dot{\varepsilon}_{ct} > 30s^{-1}$

With $\log \beta_s = 7.112\delta_s$-2.33 log

Where $\dot{\varepsilon}_{ct}$ is the strain rate (s^{-1})

$\dot{\varepsilon}_{cto} = 3 \times 10^{-6} s^{-1}$

$\delta_s = \frac{1}{10+6f_{cm}/f_{cm0}}$ with $f_{cm0} = 10\text{MPa}$

The dynamic simulations were performed for three tests by using ABAQUS/Explicit. The main parameters applied in the impact test are presented in Table 6. The impact head was modelled as a rigid body plate with the same impact area. The plate was assigned a mass of 440 kg, and the same velocity as applied to the test trolley was prescribed to ensure that the dynamic simulations have the same kinetic energy as the impact tests.

Table 6 Parameters for the Impact tests

Parameters for impact test	DHD01	DHD02	DHD03	DHD04	DHD06	DHD07
Kinetic energy in wagon [J]	3336	2549	972	1389	2460	3405
Speed [m/s]	3.89	3.40	2.1	2.51	3.34	3.93

3.5. Finite element models of the entire slab in the full-scale test

As previously described in Section 2.4, three full-scale tests (T1, T2 and T3) each consisting of two cases (F1 and F2) were performed. The test T1 and T2 had the same test setup where the length of the impactor was 10.0 m and the fall height 3.2 m, while for test T3, the impactor length was 9.7 m and the fall height was 3.6 m as shown in Table 7. The nonlinear dynamic FE analyses were performed for two cases: test T1 and T3 and in both cases F1 and F2 were simulated.

Table 7 Length of impactor and the fall height in full-scale test

Test nr.	1	2	3
L [m]	10	10	9.7
H [m]	3.2	3.2	3.6

The full-scale test setup and the FE model are shown in Figure 22. The boundary condition of the impactor at the second falling side has a great influence on the impact point. In the FE model the chain connection at second falling side was modelled using truss elements. The predicted distances between the impact point and the end of the floor slab are shown in Figure 23, and the measured and predicted distances for both test T1 and T3 have good agreement with the experiments as shown in Table 8.

The floor had three hollow core slabs which were grouted together by concrete joints with 30 mm width at the top. Contact cohesive behaviour is defined as a surface interaction property, and it is used to model the bonded interface between the concrete joints and the HCS with the possibility of damage and failure of the bond. To achieve similar robustness as in real cases, the middle channel of the hollow core slabs was grouted over a certain length at both ends.

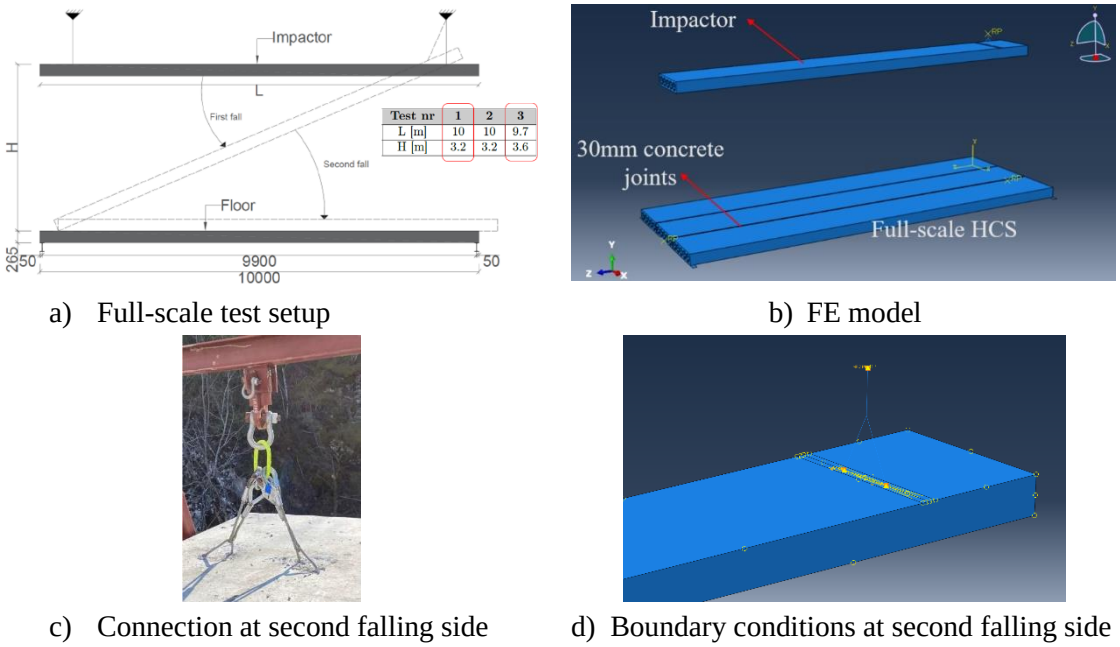

a) Full-scale test setup

b) FE model

c) Connection at second falling side

d) Boundary conditions at second falling side

Figure 22: Full-scale test of hollow core slab (HCS)

Table 8. The measured and predicted distances between the impact point and the right end of slab floor

Test nr.	Measured from test [mm]	Predicted by simulation
1	350	344
3	850	850

a) Test 1

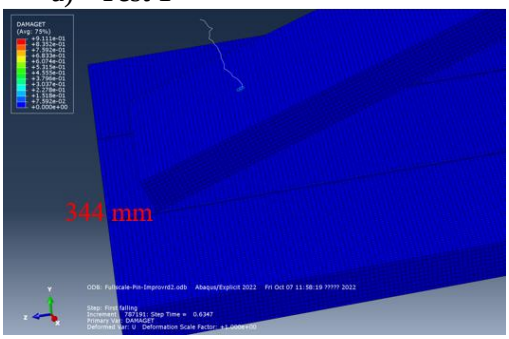

b) Test 3

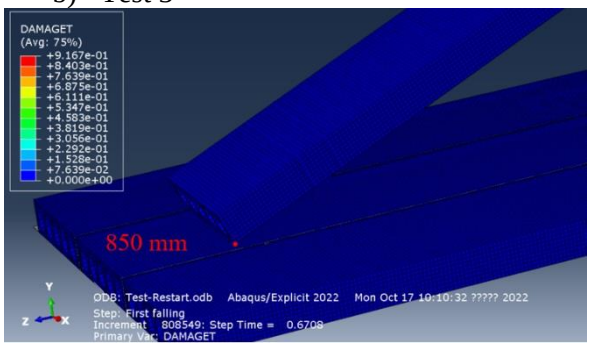

Figure 23: The distances between the impact point and the end of the floor slab predicted by the simulations.

The loads were applied in four steps in the simulation of the full-scale tests:

1) The gravity was applied initially
2) The targeted prestress was applied on the tendons through temperature changes.
3) The line which held the left side of the impactor was released to simulate the first fall.
4) The line which held the right side of impactor was released to simulate the second fall.

3.6. Nonlinear analysis of the static tests

Four different cases of the static tests on the cut-out slabs (b=0.4m & L=2.3m) with different load and support configurations, as previously considered in Chapter 4.2 and shown in Figure 24, were analysed applying both implicit and explicit equation solvers.

Two types of failure mechanisms, i.e. moment and shear failures, occurred in the tests. The dominating failure patterns in the tests are shown in Table 9, where it is seen that different failure pattern occurred for the same test setup, e.g., test HD05 and HD07 reached shear failure, while moment failure occurred in test HD06 and HD08. This means that the applied test setup is in the transition zone between moment failure and shear failure. Since the analyses similarly predict either a combined moment and shear failure or a pure shear failure, it can be concluded that the agreement between experiments and calculated concerning the failure development is reasonably good.

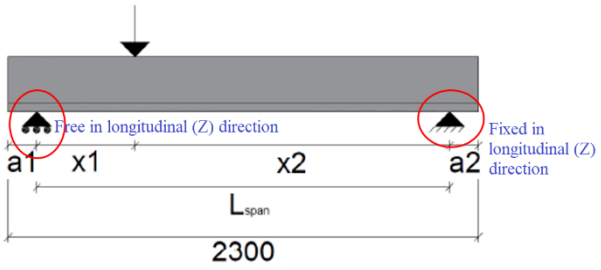

ID	01-02	03-04	05-06	07-08
a1	140	140	140	50
a2	140	140	240	630
x1	662.5	580	480	480
x2	1357.5	1440	1440	1140
L_{span}	2020	2020	1920	1620

Figure 24: Cases with concentrated load at different positions

Table 9 Dominating failure pattern

ID	Test	Simulation	
		General Static (Implicit solver)	Quasi static (Explicit solver)
HD01	Moment failure	Moment failure	Combined moment and shear failure
HD02	Moment failure		
HD03	Moment failure	Combined moment and shear failure	Combined moment and shear failure
HD04	Combined moment and shear failure		
HD05	Shear failure	Combined moment and shear failure	Combined moment and shear failure
HD06	Moment failure		
HD07	Shear failure	Shear failure	Shear failure
HD08	Moment failure		

The load-displacement relationship from the static (implicit) and the quasi-static (explicit) analyses are shown in Figure 25a)-Figure 28a) where they are compared with the test results. Although predicting the post-failure behaviour is difficult, the results are in reasonable agreement with experiments. The deviations before the 1st crack is probably due to tightening of the connection in the test rig system.

In the simulations the tensile cracking initiates when the equivalent plastic tensile strain is greater than zero, $\tilde{\varepsilon}_t^{pl} > 0$, and the maximum principal plastic strain is positive. The contour plot and the direction of the maximum principal strains from the simulations are shown in Figure 25-28 c), d) and e) and they can be compared to the corresponding DIC-recorded strains in Figures 25-28 b) and c). From the figures it is seen that in the tests it is only HD04 and HD07 that reaches a shear failure, while in the simulations significant shear cracking occurs in all cases. From the simulations it is seen that the crack occurs at the

plane which is perpendicular to the maximum principal strain as expected. Most of the failure patterns in the simulation indicates the combined moment and shear failure, i.e., the vertical cracking was first developed at the bottom of the slab at the position of the point load, and then the inclined cracking developed in the webs of the slab. In the simulations the dominating failure pattern becomes shear failure when the point load becomes closer to the right support, see e.g., test H07 and H08 where shear failure occurred. In general, the crack patterns observed in the tests and simulations had good agreement. In the explicit simulations, this may be improved by refining the mesh and adding element erosion.

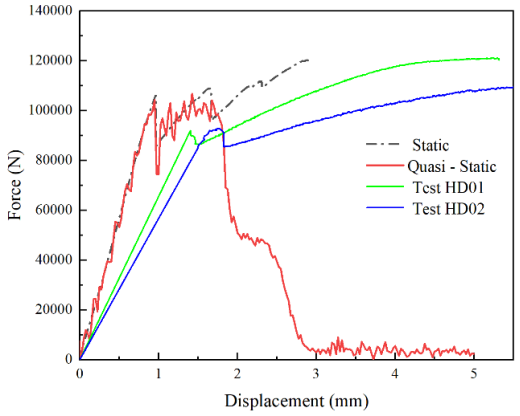

a) Load and displacement curves (HD01 and HD02)

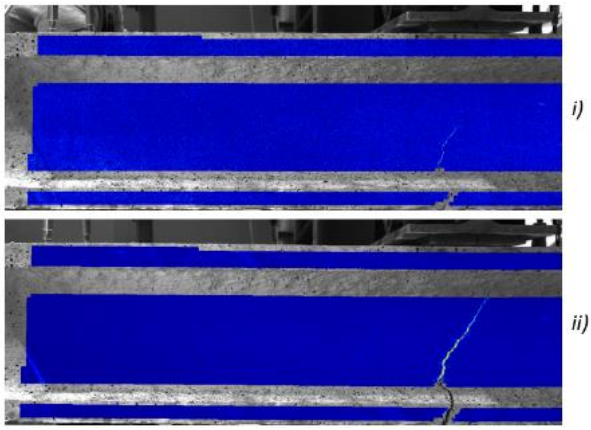

b) Strains recorded by DIC illustrating cracking and moment failure occurring in HD01(upper) and HD02.

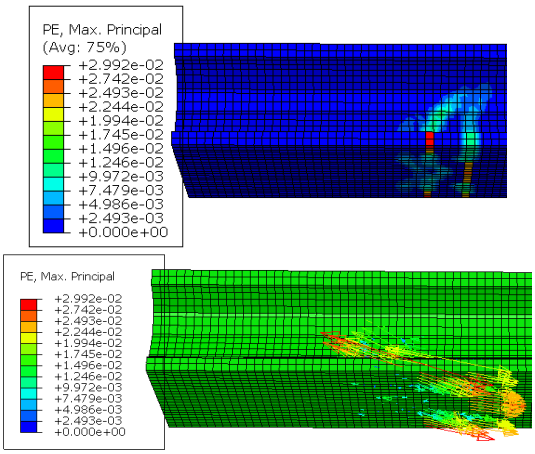

c) Size and direction of the maximum principal strains at moment failure in the static analysis

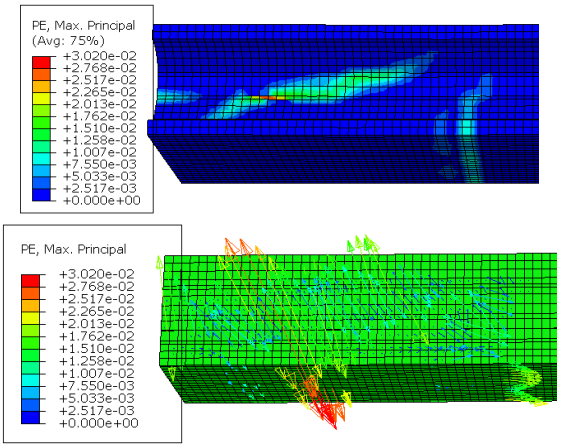

d) Size and direction of the maximum principal strains at combined moment and shear failure from the Quasi-static analysis.

Figure 25: The load-displacement curves and failure patterns of the HC cut-outs according to static tests and maximum principal strains from the numerical simulations (HD01 and HD02)

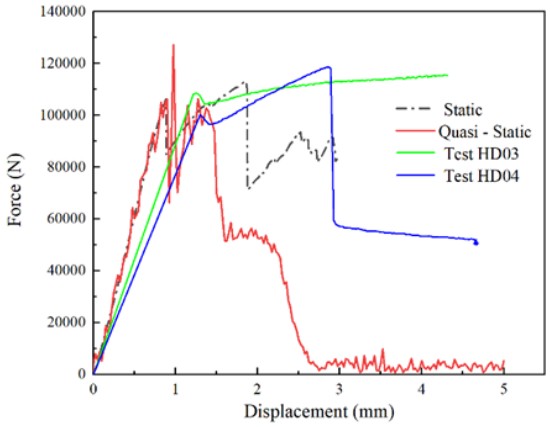

a) Load and displacement curve (HD03 and HD04)

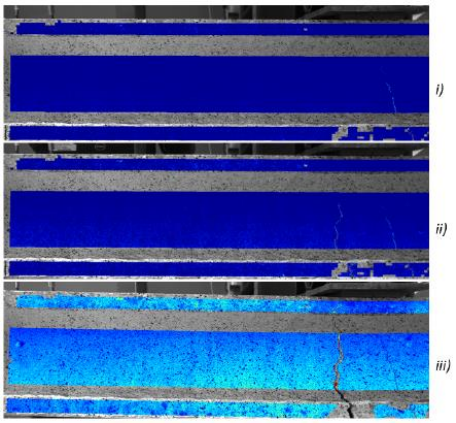

b) DIC recorded strains in test HD03 illustrating cracking and moment failure

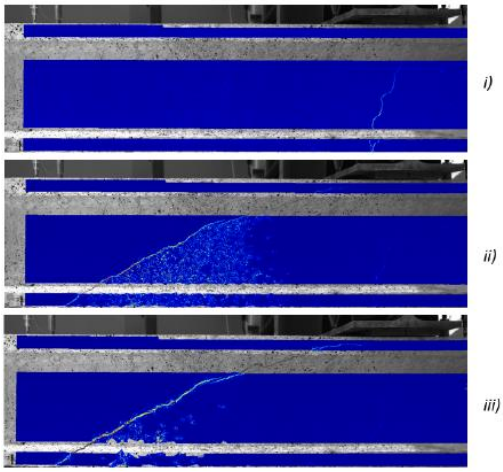

c) Recorded strains in HD04 getting combined moment and shear failure

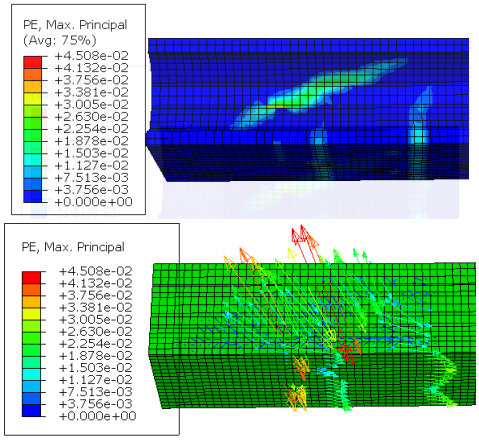

d) Size and direction of the maximum principal strains at combined moment and shear failure (static analysis)

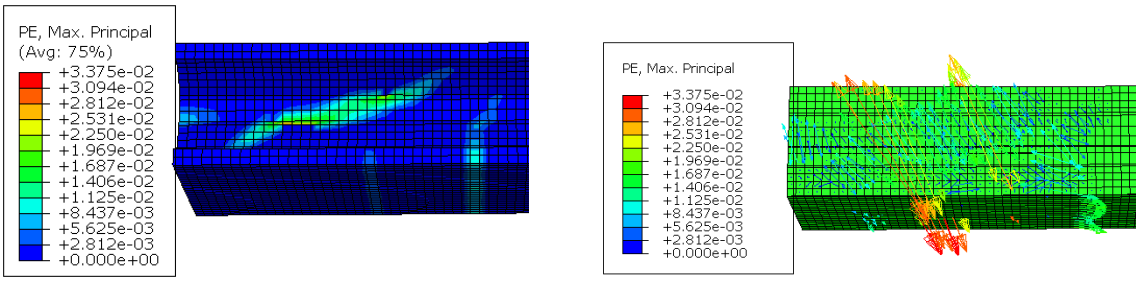

e) Size and direction of the maximum principal strains at combined moment and shear failure (Quasi static analysis)

Figure 26: The load-displacement curve and failure pattern of HCS according to static tests and simulations (HD03 and HD04)

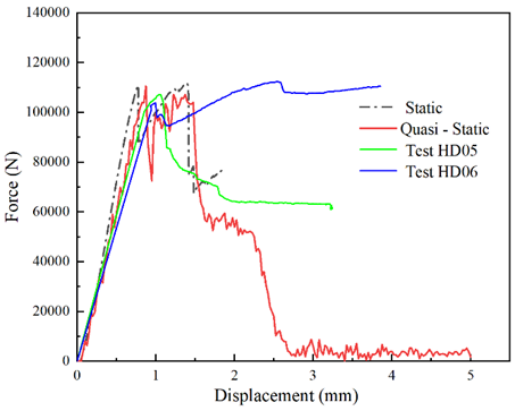

a) Load and displacement curve (HD05 and HD06)

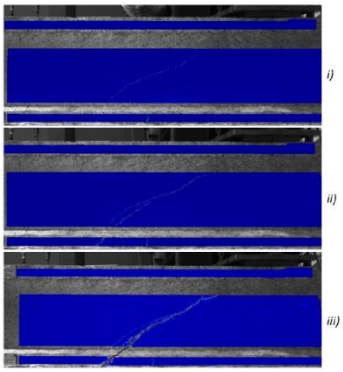

b) Crack recorded by DIC in test HD05 getting shear failure

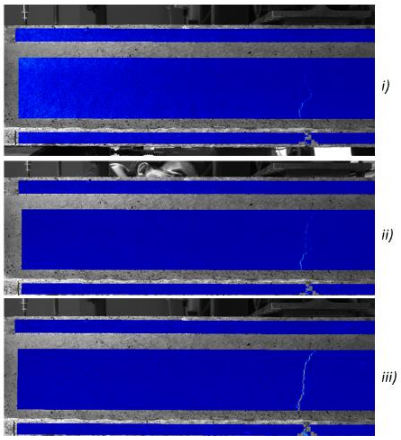

c) Crack recorded by DIC in test HD06 getting moment failure

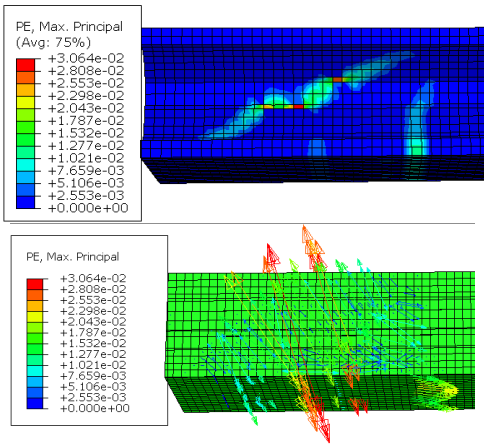

d) Size and direction of the maximum principal strains at combined moment and shear failure in the static analysis

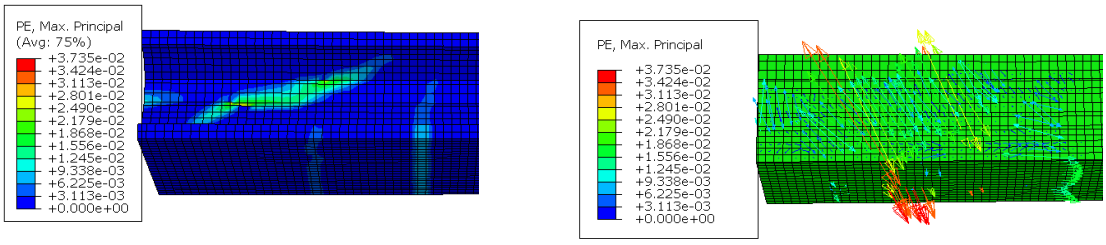

e) Size and direction of the maximum principal strain at combined moment and shear failure from the Quasi static analysis

Figure 27: The load-displacement curve and failure pattern of HCS according to static tests and simulations (HD05 and HD06)

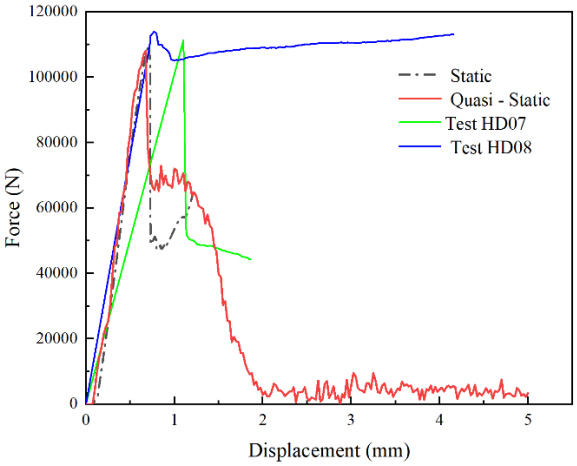

a) Load and displacement curve (HD07 and HD08)

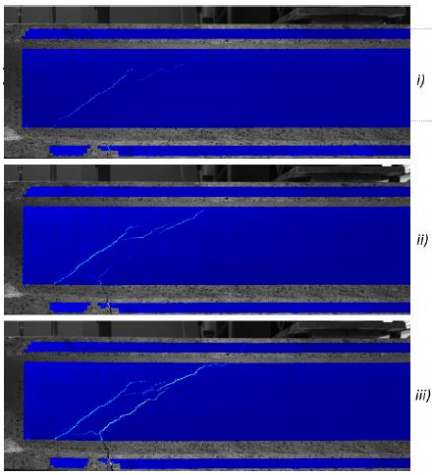

b) Cracking recorded by DIC in test HD07 where shear failure occurred

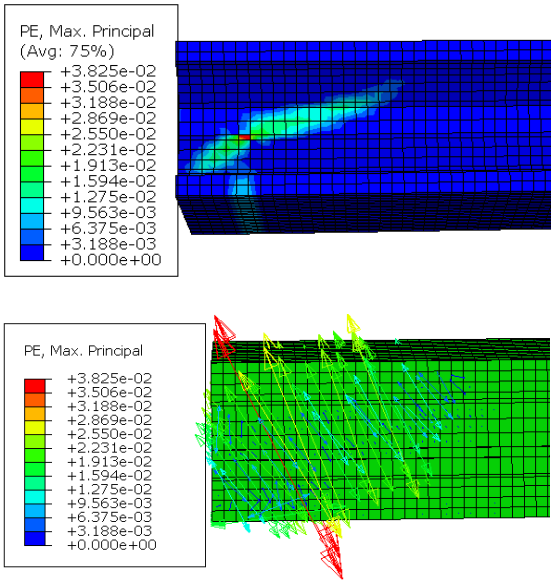

c) Size and direction of the maximum principal strain at shear failure in the static analysis

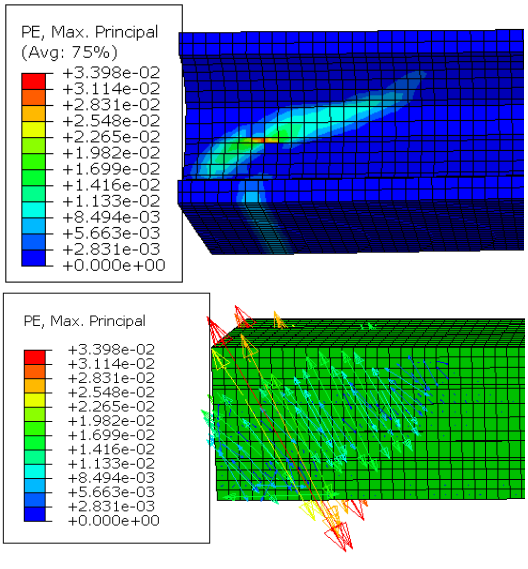

d) Size and direction of the maximum principal strain at shear failure form the Quasi static analysis

Figure 28: The load-displacement curve and failure pattern of HCS according to static tests and simulations (HD07 and HD08)

3.7. Nonlinear dynamic analysis of the impact tests

The nonlinear dynamic analyses were performed for 6 different dynamic impact tests by using the explicit equation solver. The kinetic energy (mass and velocity) is the same in the experiments and the simulations, and from Table 10 and Figure 29 it is seen that the displacement versus time curves are in reasonable agreement with the experimental data. From Table 10 it is also interesting to see that shear failures (cracking) develop in all the analyses, while this occurs only in the three tests with largest kinetic energy. In the three remaining tests chosen for simulation, only flexural cracks occurred.

The tests with lower velocity and smaller kinetic energy, DHD03, 04 and 06, reached moment cracking while in the tests with higher speed and larger kinetic energy, DHD01, 02 and 07, shear failure (cracking) occurred. In the simulations the main failure pattern is shear failure for all cases although initially flexural cracking appeared. The failure patterns in the test and the simulation for test DHD02 are shown in Figure 30, while the failure pattern in the simulation of test DHD03 is shown in Figure 31.

The contact forces at the impact area from the simulations of the tests DHD01, 02 and 03 are shown in Figure 32. The forces obtained from the simulations appear to be notably higher (2600 kN) than what was recorded in the first dynamic impact test (about 800 kN) where the load cell was destroyed.

Table 10 Input parameters and results of Impact test and simulation

Test ID	Kinetic energy in wagon [J]		Velocity [m/s]	Maximum deformation at the load point		Failure/Cracking pattern	
	Test	Simulation	Test and simulation	Test	Simulation	Test	Simulation
DHD01	3336	3329	3.89	21.6	19.9	Shear	Shear
DHD02	2549	2543	3.40	15.4	15.0	Shear	Shear
DHD03	972	970	2.10	3.8	6.7	Moment	Shear
DHD04	1389	1386	2.51	6.0	8.9	Moment	Shear
DHD06	2460	2454	3.34	9.3	15.0	Moment	Shear
DHD07	3405	3398	3.93	25.1	20.2	Shear	Shear

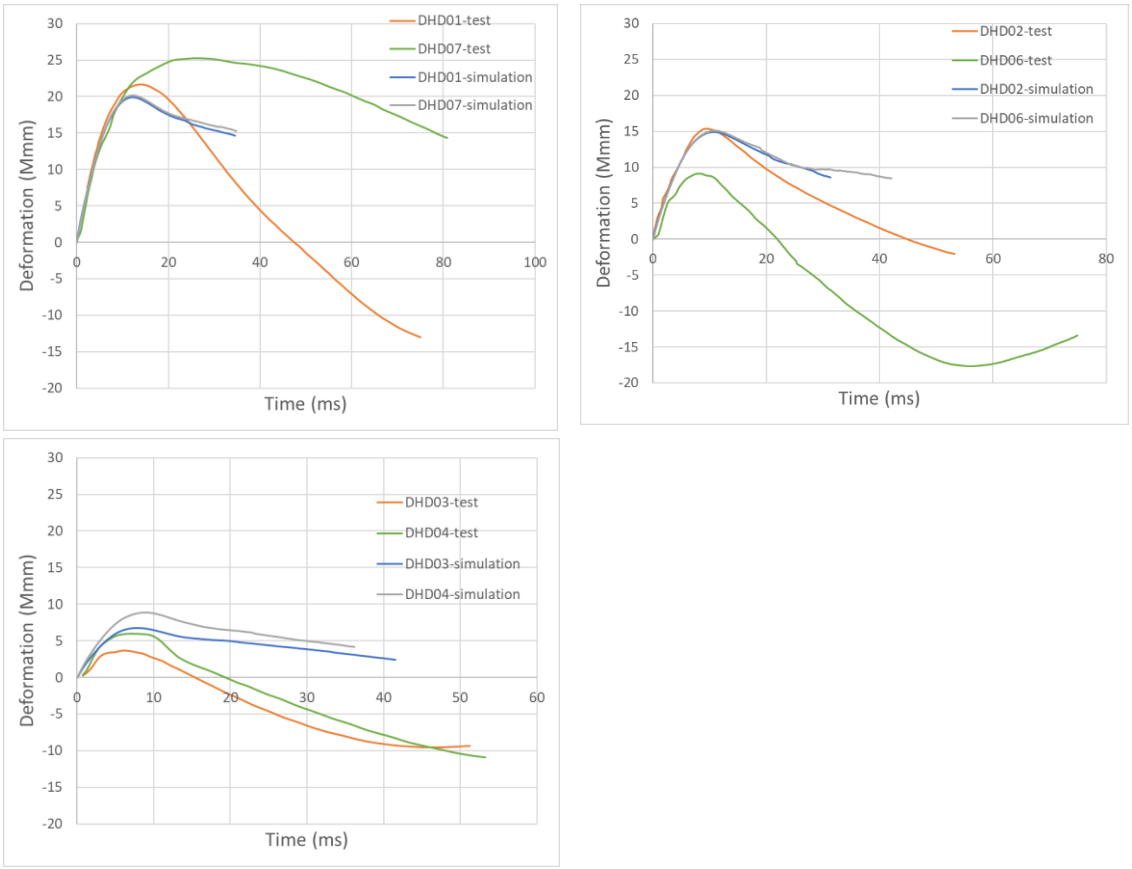

Figure 29: Deformation at the load point during the impact tests.

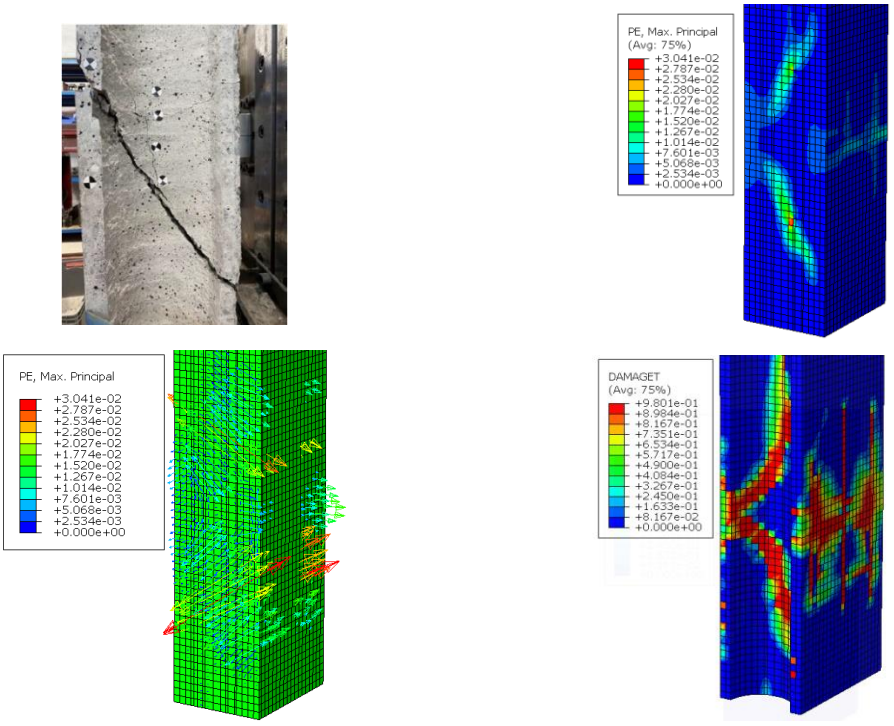

Figure 30: Failure pattern in the test and simulations for test DHD02

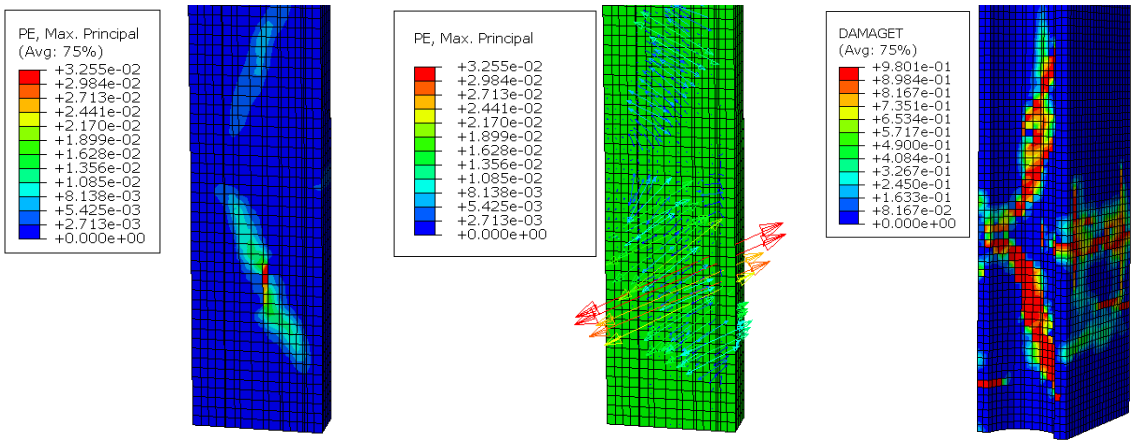

Figure 31: Failure pattern in the simulation of test DHD03

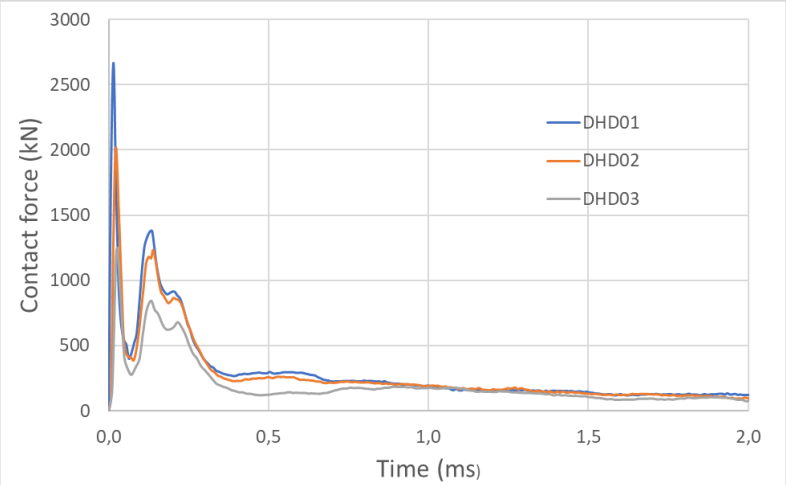

Figure 32: Contact force of the impact plate from the simulations

3.8. Nonlinear dynamic analysis of the full-scale test

Dynamic simulations were performed for the full-scale tests T1 and T3 by using the explicit solver.

The comparisons of the simulation and the first full-scale test after the first impact (T1F1) are shown in Figure 33 and Figure 34 for the impactor and the floor slab respectively. From the first figure it is seen that relatively good agreement between test and simulation is achieved for the failure pattern of the impactor. In the test the floor slab did not show visible damage at the top surface of the impact area after the first impact while the simulation results showed minor damage at the top surface of the middle element and also some damage in the web and on the bottom surface of the middle element of the floor after first impact.

The comparisons of the simulation and the first full-scale test after the second impact (T1F2) are shown in Figure 35.

The comparison of the simulation and the third full-scale test after first and second impact (T3F1 & T3F2) are shown in Figure 36 and Figure 37 respectively. The top surface of the impact area did not show visible damage after the first impact which agrees with the simulation results. The deformation predicted by simulation has good agreement with the measured one from test at location 3.75 m from left support as shown in Figure 38.

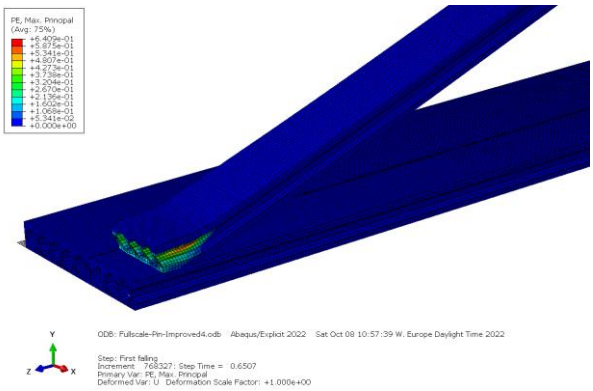

a) Maximum principal strain

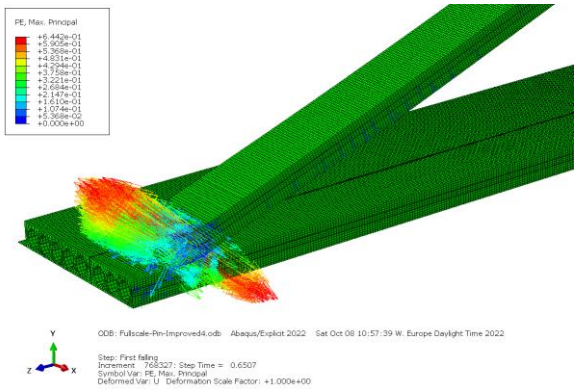

b) Direction of maximum principal strain

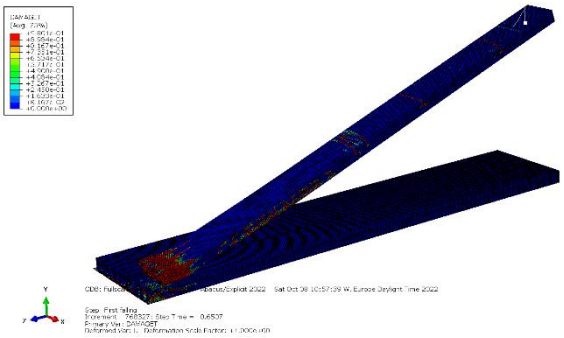

c) Tensile damage viwed from top side of impactor

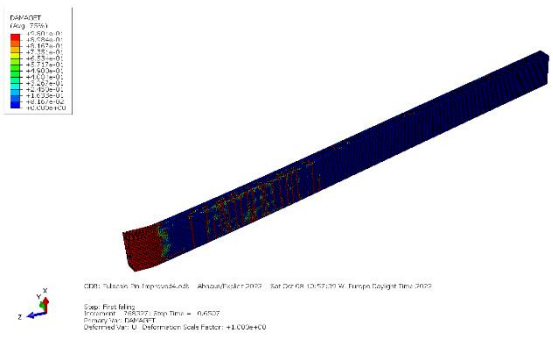

d) Tensile damage viewed from the bottom side of impactor

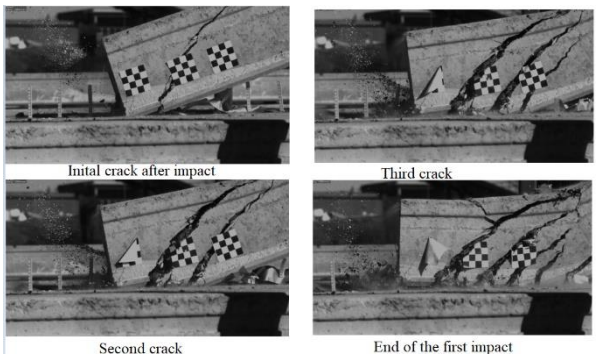

e) Crack development during the first impact

f) The front of impactor after the first impact

Figure 33: Comparison between simulation and test for the impactor after the first fall for full-scale test 1 (T1F1)

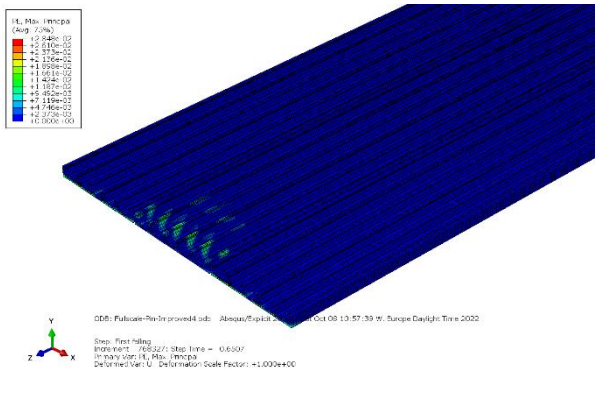

a) Maximum principal strain

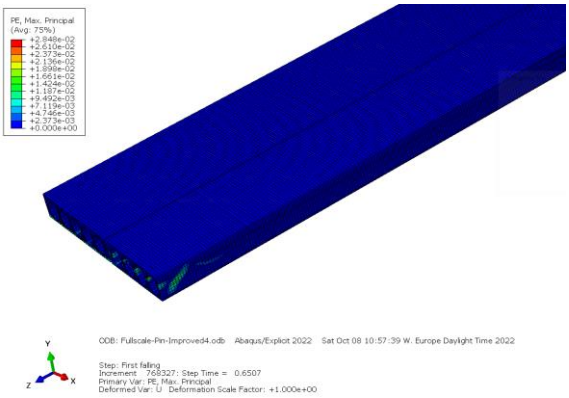

b) Maximum principal strain at web of floor slab (Symmetric half)

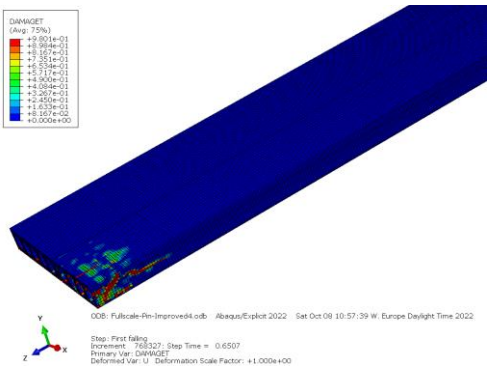

c) Tensile damage viewed from the top side of the floor slab (symmetric half)

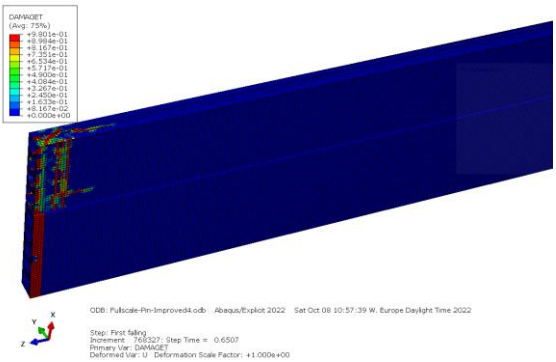

d) Tensile damage viewed from the bottom side of the floor slab

e)Top surface of the impact area after the first impact

Figure 34: Comparison between simulation and test for the floor slab after the first fall for full-scale test 1 (T1F1)

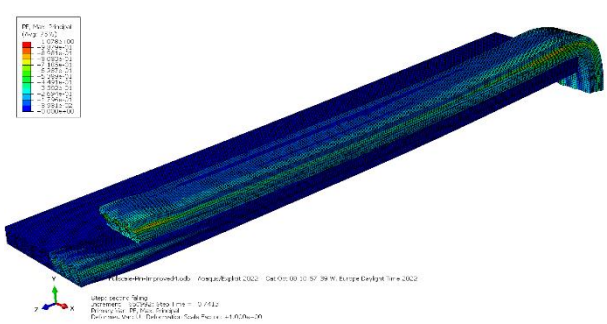

a) Maximum principal strain after the second impact

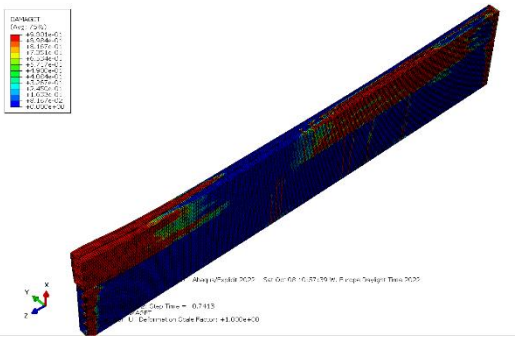

b) Tensile damage at floor slab after the second impact

c) Area around the support at right side after the second impact

d) The end of impactor after the second impact

Figure 35: Comparison between simulation and test after the second fall for the full-scale test 1 (T1F2)

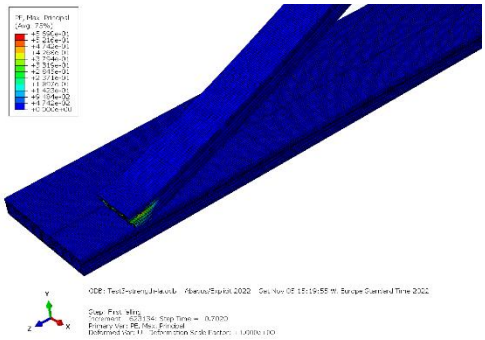

a) Maximum principal strain

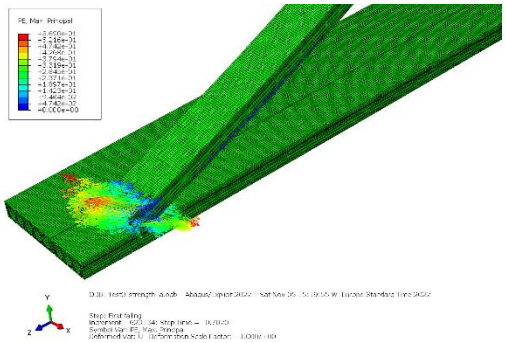

b) Direction of maximum principal strain

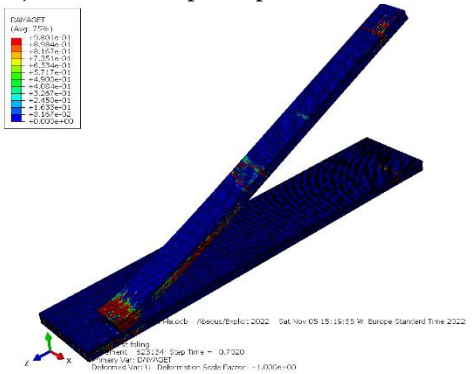

c) Tensile damage after the first impact

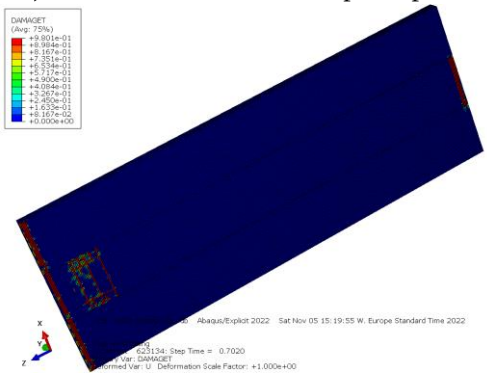

d) Tensile damage at the bottom surface of floor slab after the first impact

Initial crack

End of first impact

Second crack

e) Crack development in the impactor during the first impact

f) The end of impactor after the first impact

g) Top surface of the impact area after first impact

Figure 36: Comparison between simulation and test after the first fall for full-scale test 3 (T3F1)

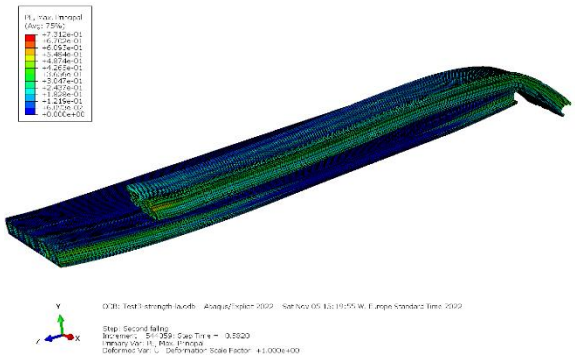

a) Maximum principal strain after second impact

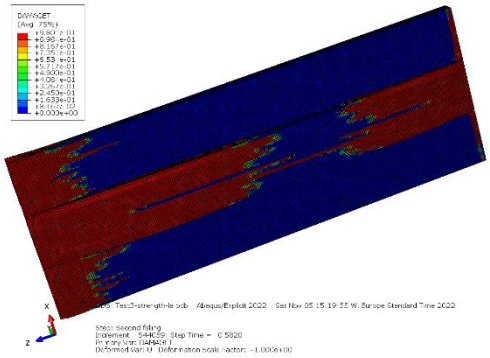

b) Tensile damage at the bottom surface of the floor slab after the second impact

c) The area close to the support at right side after second impact

Figure 37: Comparison between simulation and test after the second impact for full-scale test 3 (T3F2)

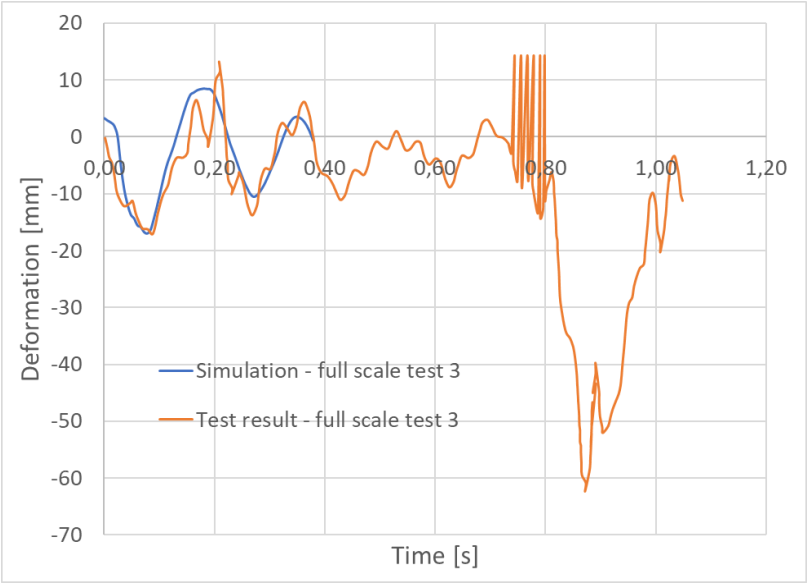

Figure 38: The deformation at location 3.75 m from the left support

4. Summary and conclusions

A series of laboratory and full-scale field tests were carried out to investigate the structural behaviour of hollow core slabs in the assembly stage. The performed full-scale test consisted of two cases: The planned Fall 1 and the unintended Fall 2. The test set up is not «a copy» of the accidental situations that previously have occurred in Trondheim and Oslo, instead it should be interpreted as one possible (and most likely) accidental situation. Although the results from the unintended Fall 2 are also interesting, an accident like that has never occurred in real life. The probability of thi scenario is therefore very low.

The intention was to establish a basis for evaluation of the current regulations and practice concerning allowance of work at story levels below floors where hollow core slabs are being assembled. Nonlinear finite element analyses using the software system ABAQUS were applied to simulate the structural behaviour and establish a theoretical basis for further investigations. The results and experience gained allow us to draw the following conclusions:

- The experimental program is original and was carried out in a successful way and has led to interesting results.

- The static test results compared to the regulations show that HC elements has considerable additional safety for shear failure

- The dynamic tests showed that single hollow cores are sensitive to falling loads that do not absorb energy in the impact (rigid falling objects)

- The grouted and anchored HC slab has sufficient strength to withstand the planned load case denoted Fall 1 in this report

-The grouting and anchoring works well and contributes to considerably improved strength, ductility and robustness of the hollow core slab system

- The second fall was not planned, and although the damages on the three jointed hollow core elements were severe, the test did not result in progressive collapse. Therefore, an accident like this will probably not lead to progressive collapse of a building in the assembly stage given that the regulations concerning finished floors (with grouted and anchored elements according to NS-EN 1992-1-1 9.10.2.3) below the hollow core montage are followed

- The project group is capable of simulating the structural behaviour of all the investigated cases by using nonlinear finite element analysis (NLFEA) with good accuracy

- The project has contributed to better understanding of the relevant problem

References

[1] Standard Norge. «NS-EN 12390: Prøving av herdnet betong».

[2] Egil Fagerholt. «eCorr v4.0 Documentation». https://folk.ntnu.no/egilf/ecorr/doc/

[3] CEN (European Committee for Standardization). Precast concrete products – Hollow core slab. EN-1168, 2011.

[4] A.G. Hanssen, T. Auestad, T. Tryland, M. Langseth. "The kicking machine: A device for impact testing of structural components", *International Journal of Crashworthiness* **8**(4) (2003), pp. 385–392.

[5] Dassault Systèmes. "ABAQUS User's Manual, version 2022".

[6] J. Lubliner, J. Oliver, S. Oller, E. Oñate. "A plastic-damage model for concrete", *International Journal of Solids and Structures* **25** (1989), pp. 299–326.

[7] J. Lee, G.L. Fenves. "Plastic-damage model for cyclic loading of concrete structures", *Journal of Engineering Mechanics* **124** (1998), pp. 892–900.

[8] Comite Euro-International du Beton, CEB-FIP Model Code 1990, Thomas Telford Services Ltd, 1993 (ISBN 0-7277-1696-4).